J Neurophysiol 114: 3177–3200, 2015.
First published September 2, 2015; doi:10.1152/jn.00324.2015.

Functional differentiation of cholinergic and noradrenergic modulation in a biophysical model of olfactory bulb granule cells

Guoshi Li,[1] Christiane Linster,[2] and Thomas A. Cleland[1]
[1]*Department of Psychology, Cornell University, Ithaca, New York;* [2]*Department of Neurobiology and Behavior, Cornell University, Ithaca, New York*

Submitted 30 March 2015; accepted in final form 1 September 2015

Li G, Linster C, Cleland TA. Functional differentiation of cholinergic and noradrenergic modulation in a biophysical model of olfactory bulb granule cells. *J Neurophysiol* 114: 3177–3200, 2015. First published September 2, 2015; doi:10.1152/jn.00324.2015.— Olfactory bulb granule cells are modulated by both acetylcholine (ACh) and norepinephrine (NE), but the effects of these neuromodulators have not been clearly distinguished. We used detailed biophysical simulations of granule cells, both alone and embedded in a microcircuit with mitral cells, to measure and distinguish the effects of ACh and NE on cellular and microcircuit function. Cholinergic and noradrenergic modulatory effects on granule cells were based on data obtained from slice experiments; specifically, ACh reduced the conductance densities of the potassium M current and the calcium-dependent potassium current, whereas NE nonmonotonically regulated the conductance density of an ohmic potassium current. We report that the effects of ACh and NE on granule cell physiology are distinct and functionally complementary to one another. ACh strongly regulates granule cell firing rates and afterpotentials, whereas NE bidirectionally regulates subthreshold membrane potentials. When combined, NE can regulate the ACh-induced expression of afterdepolarizing potentials and persistent firing. In a microcircuit simulation developed to investigate the effects of granule cell neuromodulation on mitral cell firing properties, ACh increased spike synchronization among mitral cells, whereas NE modulated the signal-to-noise ratio. Coapplication of ACh and NE both functionally improved the signal-to-noise ratio and enhanced spike synchronization among mitral cells. In summary, our computational results support distinct and complementary roles for ACh and NE in modulating olfactory bulb circuitry and suggest that NE may play a role in the regulation of cholinergic function.

acetylcholine; norepinephrine; olfactory bulb; computational model; neuromodulation

NEUROMODULATORS such as norepinephrine (NE), acetylcholine (ACh), and serotonin serve important functions in sensory perception. These neuromodulatory systems have variously been ascribed specific and often overlapping functions in sensory systems, including improving neuronal signal-to-noise ratios (SNRs), governing attentional processes and general systemic arousal, and regulating learning and memory mechanisms (Aston-Jones and Cohen 2005; Cools et al. 2008; Sarter and Bruno 1997; Sarter et al. 2005; Schultz et al. 1997; Usher et al. 1999). Achieving clear functional dissociations among the roles of these modulators in sensory processing is not trivial and warrants further investigation. Indeed, recent studies have begun to dissociate distinct functions for noradrenergic and cholinergic projections to the olfactory bulb (OB) despite substantial overlap in their modulatory effects on particular neurons. Behaviorally, both neuromodulators influence the discrimination of similar odorants in adult mice and rats (Doucette et al. 2007; Mandairon et al. 2006, 2008). ACh, in particular, strongly modulates the differentiation of similar odors by regulating OB circuits to increase contrast between highly similar odorant representations (Chaudhury et al. 2009; Devore and Linster 2012; Devore et al. 2012; Linster and Cleland 2002; Mandairon et al. 2006). In contrast, only NE produced a behavioral effect on the processing of very-low-concentration odorants, substantially lowering the detection and discrimination thresholds for weak odor stimuli (Escanilla et al. 2012).

The OB receives extensive cholinergic inputs from the horizontal limb of the diagonal band of Broca (Záborszky et al. 1986). ACh in the OB acts on both nicotinic and muscarinic receptors (Castillo et al. 1999; Ghatpande et al. 2006; Pressler et al. 2007), which are substantially segregated to different OB layers; nicotinic receptors are typically located within the glomerular and mitral cell (MC) layers, whereas muscarinic receptors are located in the granule cell (GC) layer and in the external plexiform layer (EPL), within which GCs and MCs interact synaptically. In vitro, the activation of nicotinic receptors has been shown to depolarize MCs (Castillo et al. 1999; D'Souza and Vijayaraghavan 2012); earlier in vivo studies also suggested that activation of nicotinic receptors would increase firing in periglomerular cells (Ravel et al. 1990), a finding that has been supported by recent slice data (D'Souza and Vijayaraghavan 2012). Muscarinic receptor activation increases the excitability of GCs by transforming a net afterhyperpolarization (AHP) following each spike into an afterdepolarization (ADP) (Pressler et al. 2007; Smith and Araneda 2010). This ADP extends the period of activation of the GC, altering the balance of excitation and inhibition in the deeper bulbar layers and constraining MC action potential (AP) timing (Li and Cleland 2013; Pressler et al. 2007). In concert, nicotinic and muscarinic cholinergic inputs depolarize MCs while enhancing both periglomerular inhibition of MC primary dendrites and GC inhibition of MC secondary dendrites (D'Souza and Vijayaraghavan 2012). The net effect of this cholinergic modulation improves the temporal precision of MC APs and increases the specificity of MC odor responses (de Almeida et al. 2013; Li and Cleland 2013; Mandairon et al. 2006).

The OB also receives a dense noradrenergic projection from the locus coeruleus that terminates in all but the most superficial layers of the bulb although preferentially targeting the GC layer and, to a lesser extent, the MC layer (McLean et al.

Address for reprint requests and other correspondence: G. Li, Dept. of Psychiatry, University of North Carolina, 4129 Neuroscience Research Bldg., 111 Mason Farm Rd., Chapel Hill, NC 27599-7250 (e-mail: guoshi_li@med.unc.edu).

Table 1. *Conductance densities and distribution of ionic currents in the granule cell model under nonmodulated control conditions*

	I_L	I_{KL}	I_{Na}	I_{DR}	I_A	I_M	I_H	$I_{CaP/N}$	I_{CaT}	I_{CAN}	I_{AHP}
Soma	0.056	0.15	100	9	—	0.23	—	—	—	—	—
Dendrites and Spine	0.056	—	35	3	13	—	0.1	0.2	0.1	0.8	0.23

Values are in mS/cm^2.

1989). Each of the three major NE receptor subtypes (α1, α2, and β) is expressed in multiple layers of the OB, and individual OB neurons can express multiple NE receptor subtypes. In vitro data from adult rodent OB show that α1- and α2-receptor activations have opposing effects on GCs; α2-receptor activation reduces while α1-receptor activation increases the rate of spontaneous inhibitory postsynaptic currents. Because α2-receptors have a higher affinity for NE than α1-receptors, α2-receptor effects dominate at very low concentrations of NE (Nai et al. 2009, 2010). With increasing concentrations of NE, α1-receptor effects come to dominate the α2-mediated effects in GCs, increasing their inhibition of MCs while also directly depolarizing MCs (Hayar et al. 2001; Nai et al. 2009; Zimnik et al. 2013). The net result appears to be an enhancement of neuronal SNRs and improved detection of very-low-concentration odorants (Escanilla et al. 2010). Activation of β-receptors does not appear to significantly modulate GC activity in adult mice (Zimnik et al. 2013).

Although several of the cellular effects of ACh and NE on bulbar neurons, particularly GCs, are superficially similar, they differ in key details and in the concerted patterns of coactivation that regulate neural circuit transformations. We here develop biophysical models of OB GCs and the local microcircuit in which they are embedded to investigate the basis for the functional differences of NE and ACh modulatory effects on OB neuronal and network function.

METHODS

The GC model. The GC model was adapted from that of Li and Cleland (2013), comprising four compartments (soma, radial dendrite, spine shaft, and spine body) and containing nine active ionic currents plus two ohmic leak currents. Detailed descriptions of compartmental dimensions can be found in Li and Cleland (2013). The values for the specific membrane resistance, membrane capacitance, and cytoplasmic (axial) resistivity were, respectively, $R_m = 18$ KΩ/cm^2, $C_m = 2$ μF/cm^2, $R_a = 80$ Ω·cm. The leak reversal potential (E_L) was set to -60 mV, and the resting potential (V_{rest}) was -68 mV. The input resistance (R_{IN}) was ~900 MΩ at rest, and the membrane time constant $\tau_m = R_m C_m = 36$ ms, all consistent with experimental data (Nai et al. 2010; Pinato and Midtgaard 2003; Pressler et al. 2007; Schoppa and Westbrook 1999). In common with the 2013 model, the GC contained a fast, spike-generating sodium current (I_{Na}), a potassium-delayed rectifier (I_{DR}), a transient A-type potassium current (I_A), a noninactivating muscarinic potassium current (I_M), low-threshold inactivating (I_{CaT}) and high-threshold ($I_{CaP/N}$) calcium currents, a Ca^{2+}-activated nonspecific cation current (I_{CAN}), and a Ca^{2+}-dependent potassium current (I_{AHP}). In addition, the present model contained a hyperpolarization-activated current (I_H) and an ohmic potassium current (I_{KL}) that was modulated by NE (Nai et al. 2010; Tables 1, 2, and 3). The ohmic potassium current was modeled as $I_{KL} = g_{KL}(V - E_K)$, with the default value $g_{KL} = 0.15$ mS/cm^2. All other active conductance kinetics were modeled using Hodgkin-Huxley-like equations (Hodgkin and Huxley 1952; Table 4). Specifically, the ionic current for a given channel i, I_i, was modeled as $I_i = g_i m^p h^q (V - E_i)$, where g_i was its maximal conductance, m its activation variable (with exponent p), h its inactivation variable (with exponent q), and E_i its reversal potential. The I_{CAN} current utilized a slightly modified equation (Inoue and Strowbridge 2008): $I_{CAN} = g_{CAN} M([Ca]_i) m (V - E_{Cation})$, where $M([Ca]_i) = [Ca]_i/(200 + [Ca]_i)$ is a Michaelis-Menten function and $[Ca]_i$ indicates the intracellular calcium concentration. The kinetic equation for the gating variable x (m or h) satisfied a first-order kinetic model

$$\frac{dx}{dt} = \phi_x \frac{x_\infty(V) - x}{\tau_x(V)} \quad (1)$$

where ϕ_x was a temperature-dependent factor (defined at 35°C), x_∞ was the voltage-dependent steady state, and τ_x was the voltage-dependent time constant (in ms). Equivalently, *Eq. 1* can be written as:

$$\frac{dx}{dt} = \phi_x(\alpha_x(V)(1 - x) - \beta_x(V)x) \quad (2)$$

where α_x and β_x are voltage-dependent rate constants with dimensions of ms^{-1}. The maximum conductance densities for all currents are shown in Tables 1–3, whereas all GC ion channel kinetics parameters are listed in Table 4. The sodium, potassium, and calcium reversal potentials were set to be $E_{Na} = 50$ mV, $E_K = -80$ mV, and $E_{Ca} = 100$ mV. The reversal potentials for the I_H and I_{CAN} currents were $E_H = -30$ mV (Cadetti and Belluzzi 2001) and $E_{CAN} = 10$ mV (Inoue and Strowbridge 2008), respectively. Intracellular calcium was regulated by a simple first-order differential equation of the form (Li and Cleland 2013)

$$\frac{d[Ca^{2+}]_i}{dt} = -\frac{I_{Ca}}{zFw} + \frac{[Ca^{2+}]_{rest} - [Ca^{2+}]_i}{\tau_{Ca}} \quad (3)$$

where w is the shell thickness (0.2 μm), $z = 2$ is the valence of the Ca^{2+} ion, F is the Faraday constant and τ_{Ca} is the Ca^{2+} removal rate (1,000 ms; Inoue and Strowbridge 2008). The resting Ca^{2+} concentration was set to $[Ca^{2+}]_{rest} = 0.05$ μmol/l.

Microcircuit model of MC-GC interactions. To examine how the modulatory effect of ACh and NE on GCs influences the firing patterns of MCs, a small microcircuit model consisting of 2 MCs and 30 GCs was developed. Importantly, the MCs were included as a metric to assess neuromodulatory effects on GCs; model MCs them-

Table 2. *Conductance densities of the I_M and I_{AHP} currents corresponding to different CCh concentrations*

[CCh], μM	0	1	2	5	10	50
g_M, mS/cm^2	0.23	0.05	0.04	0.03	0.02	0.0
g_{AHP}, mS/cm^2	0.23	0.05	0.04	0.03	0.02	0.0

CCh, carbachol.

Table 3. *Conductance density of the ohmic potassium current, I_{KL}, corresponding to different NE concentrations*

[NE], μM	0	0.1	0.3	1	3	10
g_{KL}, mS/cm^2	0.15	0.25	0.3	0.25	0.05	0.0

NE, norepinephrine.

Table 4. *Kinetics of gating variables for each channel mechanism implemented in the GC model cell*

Current Type	Gating Variable	ϕ_x	α_x or x_∞	β_x or τ_x, ms	Ref.
I_{Na}	$p = 3$	2.1	$\alpha_m = \frac{0.4(V+18)}{1-\exp(-(V+18)/7.2)}$	$\beta_m = \frac{-0.124(V+18)}{1-\exp((V+18)/7.2)}$	Migliore et al. 2005
			$m_\infty = \alpha_m/(\alpha_m + \beta_m)$	$\tau_m = \max\{1/(\alpha_m + \beta_m), 0.02\}$	
	$q = 1$	2.1	$\alpha_h = \frac{0.03(V+33)}{1-\exp(-(V+33)/1.5)}$	$\beta_h = \frac{-0.01(V+33)}{1-\exp((V+33)/1.5)}$	
			$h_\infty = \frac{1}{1+\exp((V+38)/4)}$	$\tau_h = \max\{1/(\alpha_h + \beta_h), 0.5\}$	
I_{DR}	$p = 2$	3.3	$m_\infty = \frac{1}{1+\exp(-(V-21)/10)}$	$\tau_m = \frac{285.7\exp((V+50)/36.4)}{1+\exp((V+50)/18.2)}$	Migliore et al. 2005
I_M	$p = 1$	1	$m_\infty = \frac{1}{1+\exp(-(V+35)/5)}$	$\tau_m = \frac{1000}{3.3\exp((V+35)/40)+\exp(-(V+35)/20)}$	Bhalla and Bower 1993
I_A	$p = 1$	3.3	$m_\infty = \frac{1}{1+\exp(-(V-5.6)/14)}$	$\tau_m = \frac{25\exp((V+45)/13.3)}{1+\exp((V+45)/10)}$	Migliore et al. 2005
	$q = 1$	3.3	$h_\infty = \frac{1}{1+\exp((V+55.4)/6)}$	$\tau_h = \frac{277.8\exp((V+70)/5.1)}{1+\exp((V+70)/5)}$	
I_H	$p = 1$	2.1	$m_\infty = \frac{1}{1+\exp((V+80)/10)}$	$\tau_m = \frac{1176.5\exp((V+65)/23.5)}{1+\exp((V+65)/11.8)}$	Cadetti and Belluzzi 2001
$I_{CaP/N}$	$p = 2$	1	$m_\infty = \frac{1}{1+\exp(-(V+10)/4)}$	$\tau_m = 0.4 + \frac{0.7}{\exp(-(V+5)/15)+\exp((V+5)/15)}$	Inoue and Strowbridge 2008
	$q = 1$	1	$h_\infty = \frac{1}{1+\exp((V+25)/2)}$	$\tau_h = 300 + \frac{100}{\exp(-(V+40)/9.5)+\exp((V+40)/9.5)}$	
I_{CaT}	$p = 2$	1	$m_\infty = \frac{1}{1+\exp(-(V+44)/5.5)}$	$\tau_m = 1.5 + \frac{3.5}{\exp(-(V+30)/15)+\exp((V+30)/15)}$	Inoue and Strowbridge 2008
	$q = 1$	1	$h_\infty = \frac{1}{1+\exp((V+70)/4)}$	$\tau_h = 10 + \frac{40}{\exp(-(V+50)/15)+\exp((V+50)/15)}$	
I_{CAN}	$p = 1$	1	$m_\infty = \frac{1}{1+\exp(-(V+43)/5.2)}$	$\tau_m = 1.6 + \frac{2.7}{\exp(-(V+55)/15)+\exp((V+55)/15)}$	Inoue and Strowbridge 2008
I_{AHP}	$p = 1$	1	$\alpha_m = \frac{-500\exp((V-65)/27)(0.015-[Ca]_i)}{1-\exp(-([Ca]_i-0.015)/0.0013)}$	$\beta_m = 0.05$	Bhalla and Bower 1993

Mitral cell channel kinetics are as described in Li and Cleland (2013). GC, granule cell.

selves were not directly modulated by ACh or NE. Consequently, this microcircuit model does not constitute a full network model of ACh/NE modulatory effects. The MC model was taken directly from a previous OB model (Li and Cleland 2013) and utilized without modification. Each MC formed reciprocal dendrodendritic synapses with all GCs. Specifically, the MC lateral dendrite excited each GC spine while receiving feedback inhibition from it; the point of synaptic contact of each GC on the long MC lateral dendrite was determined randomly from a uniform distribution (Li and Cleland 2013). The MC→GC synapse was mediated by both α-amino-3-hydroxy-5-methylisoxazole propionic acid (AMPA) and *N*-methyl-D-aspartate (NMDA) receptors, whereas the GC→MC connection was mediated by γ-aminobutyric acid A ($GABA_A$) receptors. All synaptic currents were modeled exactly as in Li and Cleland (2013)

$$I_{syn} = w g_{syn} s B(V)(V - E_{syn}) \quad (4)$$

where w was the synaptic weight, g_{syn} was the maximal synaptic conductance, and E_{syn} was the reversal potential. The default maximum conductances were $g_{AMPA} = 2$ nS, $g_{NMDA} = 1$ nS, and $g_{GABAA} = 2$ nS. The synaptic weights of the MC→GC and GC→MC connections were set to 2 and 3, respectively; these relative values were chosen to replicate the spontaneous and odor-evoked firing rates of MCs and GCs (and the number of spikes in each respiratory cycle) observed in in vivo whole-cell recordings (Cang and Isaacson 2003). For AMPA and NMDA currents, $E_{syn} = 0$ mV, and for $GABA_A$ currents $E_{syn} = -80$ mV (Migliore and Shepherd 2008). The function $B(V)$, which implemented the magnesium (Mg^{2+}) block for NMDA currents, was defined as follows:

$$B(V) = \left(1 + \frac{[Mg^{2+}]\exp(-0.062V)}{3.57}\right)^{-1} \quad (5)$$

(Zador et al. 1990), where the extracellular magnesium concentration was set to $[Mg^{2+}] = 1.0$ mM. For AMPA and $GABA_A$ currents, $B(V) = 1$. The gating variable s represented the fraction of open synaptic ion channels and obeyed first-order kinetics (Wang and Buzsáki 1996)

$$\frac{ds}{dt} = \alpha F(V_{pre})(1 - s) - \beta s \quad (6)$$

where the function $F(V_{pre})$ was assumed to be an instantaneous sigmoidal function of the presynaptic membrane potential, $F(V_{pre}) =$

$1/\{1 + \exp[-(V_{pre} - \theta_{syn})/\sigma]\}$, where θ_{syn} was the half-activation potential of the synapse. For AMPA/NMDA receptor currents, θ_{syn} was set to 0 mV, and for $GABA_A$ receptor currents $\theta_{syn} = -40$ mV. We set σ to be 0.2 for AMPA/NMDA currents and 2 for $GABA_A$ currents. Thus, as in the previous model (Li and Cleland 2013), excitatory synaptic transmission required MC spike propagation while inhibitory synaptic transmission was graded. The channel rate constants (α and β) were expressed as $\alpha = 1/\tau_\alpha$ and $\beta = 1/\tau_\beta$, where τ_α and τ_β were the synaptic rise and decay time constants, respectively. All synaptic time constants were the same as in the OB network model (Li and Cleland 2013), except for the $GABA_A$ receptor current, where a faster decay time constant (3 ms) was used based on recent experimental data (Inoue and Strowbridge 2008; Schoppa 2006).

Odor stimulus and random background inputs. Rodents respire at frequencies of 1.0–3.0 Hz when at rest in a familiar environment but increase their respiration rates to 4.0–12.0 Hz under a variety of circumstances such as the investigation of a novel odorant (Verhagen et al. 2007). Such active odor sampling is typically termed "sniffing". In our simulations, we modeled both a low-frequency (2.5 Hz) respiration-like input and a high-frequency (>8.0 Hz) sniffing-like input (henceforth referred to as respiratory and sniffing inputs, respectively). The respiratory input was modeled by a current stimulus composed of trains of α functions (Pressler et al. 2007). Specifically, $I_{res}(t) = I_R(t/\tau)e^{[1 - (t/\tau)]}$ with $\tau = 60$ ms. In contrast, rather than being phasic and repeating with each sniff, olfactory receptor neuron inputs to glomeruli during high-frequency sniffing appear as largely tonic calcium signals that attenuate over time (Verhagen et al. 2007). Accordingly, the high-frequency (>8.0 Hz) sniffing input was modeled by a double exponential function: $I_{sniff}(t) = I_S\bar{A}[e^{-t/\tau 1} - e^{-t/\tau 2}]$, where $\bar{A}$ was the normalization constant chosen so that $I_{sniff}(t)$ assumes a maximum value of I_S, and $\tau_1 = 50$ ms and $\tau_2 = 3{,}000$ ms were the rise and decay time constants, respectively. These parameters were based on experimental observations (Verhagen et al. 2007); however, other studies have reported temporal modulation of MC activity at sniffing frequencies (Carey and Wachowiak 2011). These effects could be simulated using the present model with appropriate input functions.

To study the effects of ACh and NE modulation on the GC spontaneous firing rate, random excitatory background input was delivered to the GC model in single-GC model simulations and to both MCs and all GCs in the small microcircuit model. The random input was modeled as a Poisson spike train delivered at a mean rate of 500.0 Hz (to simulate the cumulative effect of many separate background inputs). Such input was exclusively mediated by AMPA receptors modeled as an instantaneous step followed by an exponential decay with a time constant of 5.5 ms (Li and Cleland 2013).

Simulated cholinergic modulation. Activation of muscarinic ACh receptors (mAChRs) by the cholinergic receptor agonist carbachol (CCh) potentiates the excitability of GCs by transforming postspike AHPs into sustained ADPs (Pressler et al. 2007; Smith and Araneda 2010). In addition, when the membrane potential is close to firing threshold, depolarizing inputs can produce quasipersistent firing when CCh is included in the bath solution (Pressler et al. 2007). To simulate the effect of mAChR activation, we reduced the conductance densities of both the potassium M-current, I_M, and the Ca^{2+}-dependent potassium current, I_{AHP}, because these two conductances underlie the AHP responses and are blocked by CCh action (Barkai and Hasselmo 1994; Li and Cleland 2013; Madison et al. 1987; Wang 1999). The effect of increasing concentrations of CCh was thus simulated by corresponding reductions in g_M and g_{AHP} conductances (Table 2). The reductions were calibrated to reflect the experimental effects of CCh on GC physiology at 2.0 μM and 50.0 μM (Pressler et al. 2007); three additional concentrations (1.0, 5.0, and 10.0 μM) also were modeled to complete the CCh concentration profile.

Simulated noradrenergic modulation. The effects of NE on GCs are concentration dependent. Although low concentrations of NE (0.1–1.0 μM) suppress GC excitability by predominantly activating only α_2-receptors, higher concentrations of NE (e.g., 10.0 μM) increase GC excitability via the activation of α_1-receptors (Nai et al. 2010). Consistent with this, the α_1-receptor agonist phenylephrine (10.0 μM) elicits membrane potential depolarization and increases spiking activities in GCs, whereas the α_2-receptor agonist clonidine (10.0 μM) induces membrane hyperpolarization and a reduction in firing frequency (Nai et al. 2010). The same study further showed that NE and phenylephrine (10.0 μM) both elicited an inward current (or reduced an outward current), whereas clonidine elicited an outward current, both of which reversed near the potassium equilibrium potential. Accordingly, α1- and α2-receptor activation appeared to bidirectionally modulate an ohmic potassium current (Nai et al. 2010). To simulate the concentration-dependent effects of NE, we increased or decreased the maximum conductance density of the ohmic potassium current accordingly; low concentrations (0.1–1.0 μM) of NE corresponded to increased I_{KL} conductance densities, whereas high concentrations (>1.0 μM) of NE corresponded to reduced I_{KL} conductance densities relative to baseline (Table 3). In these simulations, we modeled the same five NE concentrations (0.1, 0.3, 1.0, 3.0, and 10.0 μM) as were investigated by Nai et al. (2010).

Data analysis. To compare the differential effects of CCh and NE modulation on GCs and MCs, we assessed various physiological metrics, including spontaneous and odor-evoked firing frequencies, pre- and poststimulus membrane potentials, spike latencies, SNRs, respiration coupling, and patterns of spike synchronization. In microcircuit simulations, the spontaneous firing rate was measured during the 1-s period before odor onset, whereas the odor-evoked firing rate was measured during the 2-s odor presentation. For respiratory odor input, the spike latency was defined as the timing of the first spike relative to the respiratory cycle (i.e., the onset of the α function) and averaged across all respiratory cycles. In microcircuit simulations, the spike latency was averaged between the two MCs. The SNR was defined as the ratio of the odor-evoked MC firing rate to the (prestimulus) spontaneous firing rate.

To visualize the effect of CCh and NE modulation on GC/MC spike distributions across the respiratory cycles, spike-phase distribution plots were generated by calculating GC/MC spike phases. To convert spike times to phases, the start of each respiratory cycle (i.e., the onset of the α function) was assigned a phase of 0°, and the phase of each spike was computed according to the following equation:

$$\varphi = \frac{t_{spike} - t_0}{T} \times 360^\circ \quad (7)$$

where t_{spike} is the spike time, t_0 is the start time of the respiration cycle, and T is the duration of the respiration cycle. A respiration coupling index, κ, also was calculated as previously (Li and Cleland, 2013)

$$\kappa = 1/N\sqrt{\left[\sum_{i=1}^{N}\sin(\varphi_i)\right]^2 + \left[\sum_{i=1}^{N}\cos(\varphi_i)\right]^2} \quad (8)$$

where N is the total number of MC spikes combining both MC neurons in the MC-GC microcircuit during the 2-s odor presentation. This index measures how tightly the spikes are coupled to the respiration cycle and are bounded between 0 and 1; when all the spikes have identical phase, the index achieves its maximal value of unity. Thus low values of κ indicate that spike times are relatively independent of respiratory phase, whereas higher values of κ indicate that spike times are strongly constrained by respiratory phase.

Finally, to quantify the degree of synchrony between the two MCs, a spike synchronization index (SI) was calculated based on the method of Wang and Buzsáki (1996), in which synchrony was measured by the cross correlation of the two spike trains at zero time lag. Specifically, the time interval of odor presentation was divided into 5-ms bins, and the two spike trains were given by $X(i)$

and $Y(i)$, the number of spikes in the ith bin. The spike SI was computed as

$$\mathrm{SI} = \frac{\sum_{i=1}^{K} X(i)Y(i)}{\sqrt{\sum_{i=1}^{K} X(i)\sum_{i=1}^{K} Y(i)}} \quad (9)$$

where K is the number of bins. Because the exact numbers of spike pairs falling into the same bin depend on the starting time of the first bin, we calculated the SIs with different starting times by subtracting a small offset (the offset varied from 0 to 4.5 ms with a 0.5-ms interval) from the initial time of calculation (i.e., odor onset time) and reported the maximum value. When plotting major microcircuit measures under different CCh and NE concentrations, we ran the microcircuit model with 10 different random seeds and plotted the mean with standard error to minimize the effects of noise introduced by random background inputs.

Numerical methods. Both the single-cell and microcircuit models were implemented in the neuronal simulator package NEURON (version 7.3; Carnevale and Hines 2006; Hines and Carnevale 1997), using the Crank-Nicholson integration method. The single GC model was simulated with a fixed time step of 0.01 ms, and the microcircuit was simulated with a fixed step of 0.005 ms. Shorter time steps did not change the results. Simulations were run on a Linux workstation under CentOS 5.1.

RESULTS

Effects of CCh and NE modulation on current-evoked GC responses. We first examined the effects of CCh and NE modulation on current-evoked GC spiking activities. GC responses to three graded current steps under control conditions are shown in Fig. 1*A*. In response to a weak current pulse (30 pA), only two spikes were generated within 500 ms, and there was a 139-ms latency to first spike (Fig. 1*A*, *bottom*), largely owing to activation of the I_A current (Schoppa and Westbrook 1999). With a medium current injection (50 pA), the initial delay was substantially reduced (from 139 ms to 15 ms), and the GC fired 10 spikes (over 500 ms) with frequency adaptation (Fig. 1*A*, *middle*). With a large current step (100 pA), the GC discharged tonically at 54.0 Hz with minimal latency (Fig. 1*A*, *top*).

The effects of 2.0 μM CCh modulation on depolarization-evoked GC responses are shown in Fig. 1*B*. For the weak current pulse (30 pA), the number of APs increased more than threefold over control conditions (from 2 to 7), but the initial delay was reduced only modestly, to 111 ms (Fig. 1*B*, *bottom*). The medium and large current injections evoked more modest CCh effects on spike rates; the number of spikes increased by 80% for the 50-pA current pulse (from 10 to 18; Fig. 1*B*, *middle*) and by only 18.5% for the 100-pA current injection (from 27 to 32; Fig. 1*B*, *top*). The frequency adaptation of spiking in response to 50 pA under control conditions also was eliminated. The effects of 50.0 μM CCh were similar to those of the lower concentration (Fig. 1*C*); 30 pA of current generated 9 spikes, and the latency to first spike was reduced only minimally (to 107 ms; Fig. 1*C*, *bottom*). The 50-pA current step evoked 19 APs (Fig. 1*C*, *middle*), and the 100-pA current

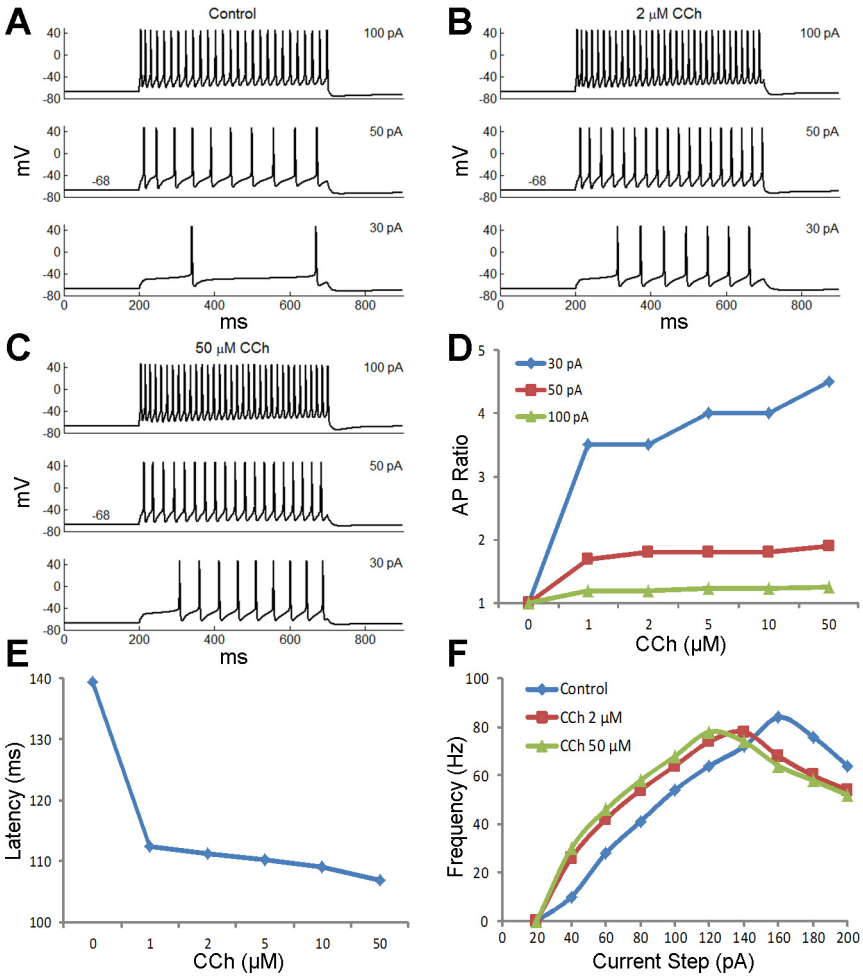

Fig. 1. Effect of the (simulated) cholinergic agonist carbachol (CCh) on current-evoked granule cell (GC) spiking activities. *A*: voltage responses of the GC model cell under baseline conditions to 3 different 500-ms current steps as indicated. Currents were applied at rest (−68 mV). *B*: as in *A*, but with 2.0 μM CCh modulation. *C*: as in *A*, but with 50.0 μM CCh modulation. *D*: ratio of action potential numbers generated under different CCh concentrations to those generated under baseline conditions, in response to each of 3 different current injection levels (30, 50, and 100 pA). *E*: latency to the first spike in response to a 30-pA current injection under different CCh concentrations. *F*: firing frequency of the GC model cell to different levels of current step under control conditions and 2.0 μM and 50.0 μM CCh modulation. Frequency was measured during the 500-ms current injection period. AP, action potential.

evoked 34 APs, again the smallest proportional increase of the 3 current levels (Fig. 1*C*, *top*). The proportional increases in the number of evoked spikes with respect to baseline/control conditions (AP ratio) arising from different concentrations of CCh application are summarized in Fig. 1*D*. Two conclusions are evident. First, the proportional effect of CCh on spike rate was most prominent for weak inputs, decreasing as input intensity increased. Second, for all current steps, the largest increase occurred at low CCh concentrations (e.g., 1.0 μM), with further increases at higher concentrations becoming considerably more marginal. Figure 1*E* depicts the initial spike latency in response to weak current input (30 pA) across all concentrations. Again, the largest effect manifested at the lowest concentrations, between 0 to 1 μM (from 139 to 112 ms, 19.4% decrease), whereas the added effects of higher concentrations were minor, and none reduced the latency below 100 ms. The reduction of spike latency was primarily a result of increased GC input resistance (which increased from 900 MΩ at baseline to 1,300 MΩ under 50.0 μM CCh), as has been observed experimentally (Pressler et al. 2007). Cholinergic neuromodulation did not affect the GC spike threshold.

The firing frequency of the GC model cell in response to a series of current steps (i.e., the *F-I* curve) is shown in Fig. 1*F* for the control, 2.0 μM, and 50.0 μM CCh conditions. For smaller current steps (up to 120 pA), CCh consistently increased firing rates at both concentrations. However, CCh also lowered the current threshold at which depolarization block (Pressler et al. 2007) was encountered, above which firing frequency was reduced owing to incomplete sodium current deinactivation. Specifically, under control conditions, depolarization block arose at >160 pA, whereas 2.0 μM CCh reduced this threshold to 140 pA, and 50.0 μM CCh reduced it further to 120 pA. Overall, CCh modulation both reduced the minimum current sufficient to initiate depolarization block and enhanced the degree of depolarization block in a concentration-dependent manner.

Concerted noradrenergic effects on model GC responses differed substantially in their concentration profiles compared with these CCh effects. On the basis of the same model cell under control conditions (Fig. 2*A*), current clamp responses of the GC model cell with the same three levels of depolarizing current and five concentrations of NE were measured. Low concentrations of NE (0.3 μM) reduced the number of APs and increased spike latency below baseline, with the largest effect observed on the weakest current input (30 pA; Fig. 2*B*). Higher concentrations of NE (10.0 μM), in contrast, increased spike rates and reduced spike latencies substantially, again most prominently observed with the weakest depolarizing input (30 pA; Fig. 2*C*), closely matching experimental data (see Fig. 4*B* from Nai et al. 2010). Moreover, unlike the effects of CCh modulation, neither low nor high NE concentrations eliminated spike frequency adaptation. This is consistent with experimental observations demonstrating that spike frequency adaptation is primarily effected by the I_M and I_{AHP} currents, neither of

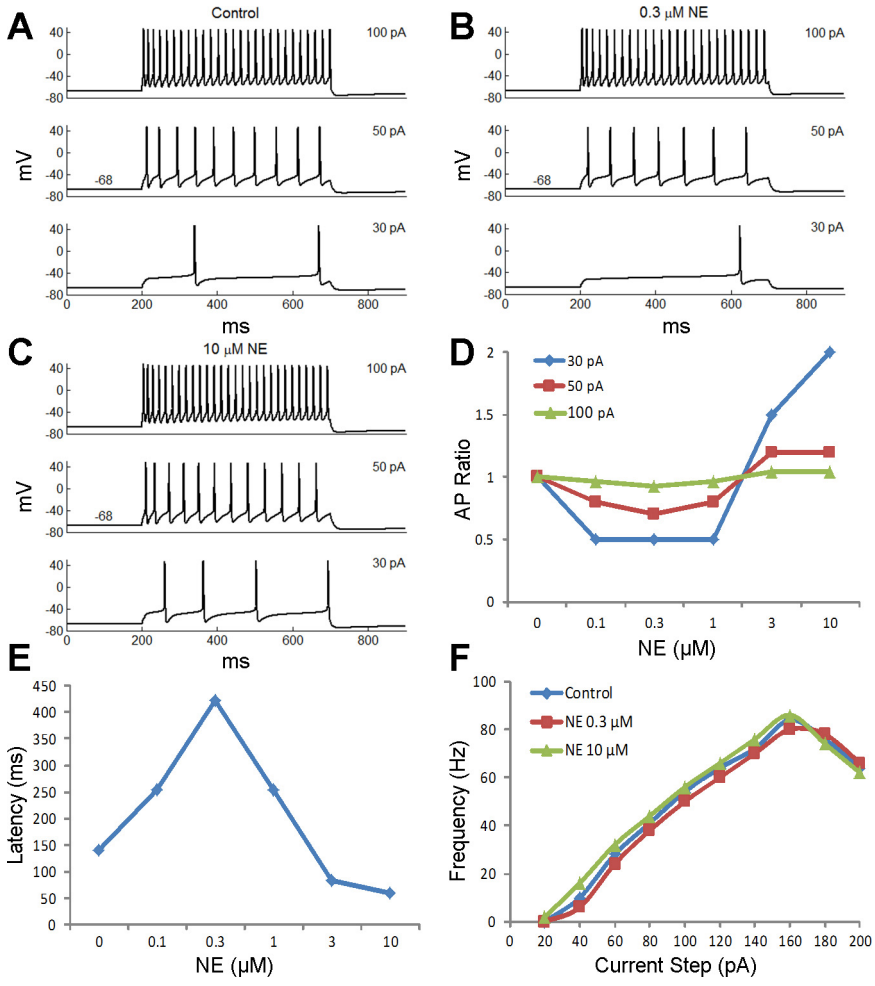

Fig. 2. Effect of norepinephrine (NE) on current-evoked GC spiking activities. *A*: voltage responses of the GC model cell under baseline conditions to 3 different 500-ms current steps as indicated. Currents were applied at rest (−68 mV). *B*: as in *A*, but with 0.3 μM NE modulation. *C*: as in *A*, but with 10.0 μM NE modulation. *D*: ratio of action potential numbers generated under different NE concentrations to those generated under baseline conditions, in response to each of 3 different current injection levels (30, 50, and 100 pA). *E*: latency to the first spike in response to a 30-pA current injection under different NE concentrations. *F*: firing frequency of the GC model cell to different levels of current step under control conditions and 0.3 μM and 10.0 μM NE modulation. Frequency was measured during the 500-ms current injection period. For *B* and *C*, small baseline currents were applied to restore the prestimulus membrane potential to the same resting value (−68 mV) because NE application alters the resting potential in GCs.

which is directly affected by NE (see Fig. 4 of Nai et al. 2010). Figure 2*D* depicts AP ratios with respect to baseline conditions across several NE concentrations and current injection levels. As with CCh, the (nonmonotonic) effect of NE modulation was most pronounced for weaker inputs (30 pA) and decreased when input intensity increased; effects on the largest current input (100 pA) were minimal. Finally, compared with CCh, NE modulation had a considerably stronger effect on spike latencies (Fig. 2*E*). Specifically, 0.3 μM NE increased spike latency threefold (from 139 ms to 422 ms), whereas 10.0 μM NE decreased spike latency more than twofold (from 139 ms to 60 ms). This effect depended primarily on the ohmic potassium current, I_{KL}, which was much more active than I_M and I_{AHP} currents in the subthreshold range (see below) and was systematically modulated by NE.

The GC *F-I* curves for the control, 0.3 μM NE, and 10.0 μM NE conditions are shown in Fig. 2*F*. Overall, NE induced much smaller effects on the *F-I* curve than did CCh (compare Figs. 1*F* and 2*F*). NE modulation did not affect the minimum current step at which depolarization block emerged, but low NE concentrations (0.3 μM) slightly attenuated the impact of the depolarization block, whereas higher NE concentrations (e.g., 10.0 μM) slightly enhanced it.

Effects of CCh and NE modulation on GC afterpotentials. One important characteristic of GCs is that they normally generate long-lasting AHP responses after spiking. These AHPs are blocked by muscarinic receptor activation, revealing a latent, long-lasting ADP, the amplitude of which increases with CCh concentration (Pressler et al. 2007). These observations were well replicated by the present model (Fig. 3, *A* and *B*). To match experimental data, we applied an AHP/ADP induction protocol identical to that of Pressler et al. (2007), in which a large depolarizing current injection (100 pA) was applied at a membrane potential of −60 mV (controlled by a baseline current). Under control conditions, a burst of spikes was evoked, producing a large AHP (peak: −12.5 mV, duration >3 s) following the termination of the current step (Fig. 3*A*, *top*). In the presence of 1 μM CCh (Fig. 3*A*, *middle*), the slow AHP was blocked completely although a fast AHP component persisted that depended primarily on the I_A and I_{DR} currents. When 2.0 μM CCh was applied (Fig. 3*A*, *bottom*), a slow ADP emerged with a peak amplitude of 3.5 mV (Fig. 3*A*, *bottom*), closely matching experimental data (mean ADP amplitude of 3.0 ± 0.8 mV; Pressler et al. 2007). When the CCh concentration was further increased to 5.0 μM, the ADP reached spike threshold (Fig. 3*B*, *top*). The number (both peak rate and duration) of ADP-induced spikes increased with further increases in CCh concentration (10.0 μM, Fig. 3*B*, *middle*; 50.0 μM, Fig. 3*B*, *bottom*), and quasipersistent firing emerged at 50.0 μM CCh (at which the I_M and I_{AHP} currents were blocked completely; Fig. 3*B*, *bottom*).

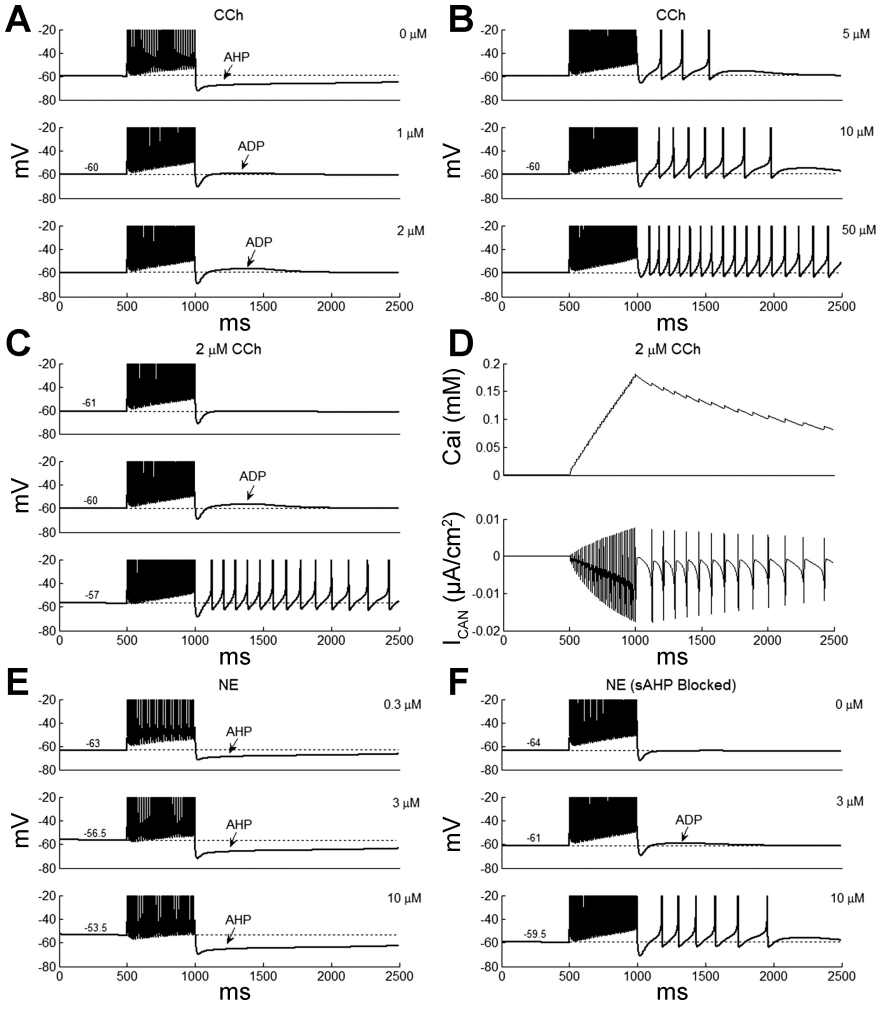

Fig. 3. Effect of CCh and NE on GC afterpotentials. *A*: effects of 3 different CCh concentrations (0, 1.0, 2.0 μM) on GC afterpotentials following a 100-pA, 500-ms current step-induced burst of spikes. Baseline membrane potential was −60 mV in all panels. *B*: higher concentrations of CCh (5.0, 10.0, 50.0 μM) generated persistent spiking atop the depolarizing afterpotential. Baseline membrane potential was −60 mV in all panels. *C*: dependence of the afterdepolarization (ADP) and persistent spiking on the prestimulus membrane potential (−61, −60, or −57 mV as indicated) in the presence of 2.0 μM CCh. *D*: time course of intracellular perimembrane Ca^{2+} concentration (*top*) and Ca^{2+}-activated nonspecific cation current (I_{CAN}) current (*bottom*) during persistent firing (2.0 μM CCh, prestimulus membrane potential was −57 mV). *E*: NE neuromodulation never produced an ADP under any concentration tested (prestimulus membrane potential was adjusted to −60 mV in the control case via current injection, and NE modulation altered the resting potential as indicated). The response under control conditions (0 μM NE) was identical to *A*, *top*. *F*: when the slow afterhyperpolarization (sAHP) was blocked by reducing the noninactivating muscarinic potassium current (I_M) and I_{AHP} currents (maximal conductances reduced from 0.23 mS/cm^2 to 0.03 mS/cm^2), high levels of NE modulation (3.0 μM and 10.0 μM) raised membrane potentials and produced sADP (*middle*) and afterpotential spikes (*bottom*) from relatively hyperpolarized membrane potential (−64 mV without modulation; *top*). In all panels, burst-inducing current steps were 100 pA × 500 ms.

The amplitude of the ADP also was dependent on the prepulse (resting) membrane potential. Under 2.0 μM CCh, when the same depolarizing current (100 pA, 500 ms) was applied from a resting potential of -61 mV, the ADP was very small (0.5 mV; Fig. 3*C*, *top*). A much larger ADP was seen when the prepulse potential was raised to -60 mV (3.5 mV; Fig. 3*C*, *middle*), and quasipersistent firing was induced following the burst when the prepulse voltage was further elevated to -57 mV (Fig. 3*C*, *bottom*), consistent with experimental observations (Pressler et al. 2007).

The ADP is dependent on intracellular calcium accumulation and mediated by the Ca^{2+}-activated nonselective cation current, I_{CAN} (Inoue and Strowbridge 2008; Pressler et al. 2007; Smith and Araneda 2010). Figure 3*D* illustrates the evolution of the intracellular perimembrane Ca^{2+} concentration (Fig. 3*D*, *top*) and the I_{CAN} current (Fig. 3*D*, *bottom*) under conditions supporting persistent firing (2.0 μM CCh, $V_{REST} = -57$ mV; corresponding to the bottom trace of Fig. 3*C*). During high-frequency burst firing, the Ca^{2+} concentration greatly increased, decaying only slowly after the end of the depolarizing current step. These sustained perimembrane calcium levels maintained a long-lasting I_{CAN} current that resulted in the persistent firing of GCs.

In contrast, no ADP emerged based on the application of NE at any concentration tested (Fig. 3*E*), and no postburst sustained firing was generated, highlighting a major difference between the functional physiological effects of CCh and NE neuromodulation. NE application did, however, alter the resting potential; 0.3 μM NE lowered it from -60 mV to -63 mV, whereas 3.0 μM and 10.0 μM NE raised it to -56.5 mV and -53.5 mV, respectively. Additionally, peak AHP amplitudes increased with higher concentrations of NE when measured from their respective prestimulus potentials (0.3 μM NE: 7.0 mV; 3.0 μM NE: 15.0 mV; 10.0 μM NE: 16.0 mV; Fig. 3*E*). These results are generally consistent with experimental data drawn from rats (Nai et al. 2010), in which neither ADPs nor persistent firing were reported under NE modulation. However, interestingly, in analogous studies performed in mouse OB slices, a submaximal concentration of NE application (10.0 μM) did produce a slow ADP (in addition to direct membrane depolarization) that could lead to quasipersistent firing, even when starting from more hyperpolarized resting membrane potentials than evoke ADPs under CCh modulation (i.e., -60 mV; Zimnik et al. 2013).

We hypothesized that this major difference between rat and mouse GC responses could have arisen from differences in their I_M and I_{AHP} conductance levels. Specifically, our base model expresses strong frequency adaptation and large AHPs, replicating experimental data drawn from rat main OB slices (Nai et al. 2010; Pressler et al. 2007) and evincing relatively large I_M and I_{AHP} conductances. In contrast, the mouse main OB GCs studied by Zimnik et al. (2013) exhibit much smaller AHP responses (1 mV AHP from a 500-ms depolarization; Figs. 1*C* and 3*A* from Zimnik et al. 2013), indicating that they express far smaller I_M and I_{AHP} conductances. Indeed, after we blocked the slow AHP in the GC model cell by reducing the I_M and I_{AHP} conductances from 0.23 mS/cm^2 to 0.03 mS/cm^2 (Fig. 3*F*, *top*), application of 3.0 μM NE depolarized the membrane potential from -64 mV to -61 mV and induced a noticeable ADP (2 mV; Fig. 3*F*, *middle*), whereas application of 10.0 μM NE depolarized the membrane potential further to -59.5 mV and produced ADP-mediated persistent spiking (Fig. 3*F*, *bottom*), a response directly comparable to experimental data from mouse main OB GCs (Fig. 3*A*2 from Zimnik et al. 2013). That is, the modulatory effect of NE in GCs depends on the magnitude of the I_M and I_{AHP} conductances, which in turn may depend on species, age, or other experimental differences. Notably, whereas our model was tuned to replicate experimental data from rat GCs expressing relatively large I_M and I_{AHP} conductances, it is not necessary to create a separate set of simulations to study GCs with low levels of I_M and I_{AHP} conductances because the effect of ACh in the model is to reduce these two conductances. Thus the modulatory effects of NE in such low-AHP GCs can be reasonably inferred from the combined CCh and NE modulation effects examined below.

Effects of CCh and NE modulation on GC spontaneous activities and membrane potentials. We next looked at the effects of CCh and NE modulation on GC spontaneous activities and membrane potentials. Driven by random background inputs, the GC model cell fired at a spontaneous mean rate of 1.6 Hz with membrane potential fluctuations (Fig. 4*A*), as reported from in vitro slice preparations (Nai et al. 2010). CCh was found to have a powerful enhancement effect on the GC spontaneous firing rate, increasing it more than 15-fold (1.6–25.0 Hz) with 2.0 μM CCh application and roughly 19-fold (to 31.0 Hz) with 50.0 μM CCh application (Fig. 4, *A* and *C*). Moreover, the spontaneous spike rate under CCh increased progressively over time (Fig. 4*A*) because the increased GC firing rate led to progressive Ca^{2+} accumulation, which in turn activated the I_{CAN} current, further exciting GCs in a positive feedback loop. This dramatic rate increase was not observed when random background input was reduced so that a positive feedback loop between Ca^{2+} accumulation and I_{CAN} activation was not formed (see microcircuit simulations below). Thus the CCh effect on GC spontaneous firing rates is clearly state-dependent, and in particular this should be taken into consideration when interpreting slice recordings.

To examine the effect of CCh on membrane potential directly, we reduced the amplitude of the random background inputs so that no spontaneous spikes were generated. Neither 2.0 μM nor 50.0 μM CCh induced a noticeable change in membrane potential with respect to baseline under these conditions (Fig. 4*B*); 2.0 μm CCh elicited a 0.23-mV depolarization, whereas 50.0 μM CCh depolarized the GC by 0.34 mV (Fig. 4*D*).

In contrast, NE had a much smaller (and nonmonotonic) effect on GC spontaneous activity levels but a much larger effect on the GC membrane potential. Application of 0.3 μM NE reduced the spontaneous mean firing rate from 1.6 Hz (in controls) to 0.2 Hz (Fig. 5*A*, *top*), whereas 10.0 μM NE increased the spontaneous spike rate almost threefold (1.6–4.4 Hz; Fig. 5*A*, *bottom*). However, with random background inputs again reduced so that no spontaneous spikes were generated under control conditions, 0.3 μM NE induced substantial membrane hyperpolarization (-3.2 mV; Fig. 5*B*, *top*), whereas 10.0 μM NE significantly depolarized the membrane ($+4.6$ mV; Fig. 5*B*, *bottom*), in sharp contrast to the negligible effect of CCh on membrane potentials (Fig. 4, *B* and *D*). The profiles of normalized spike frequency (Fig. 5*C*) and resting potential changes (ΔmV; Fig. 5*D*) across different NE concentrations closely match experimental data (Fig. 3*A* of Nai et al. 2010), validating the predictions of the model. To understand

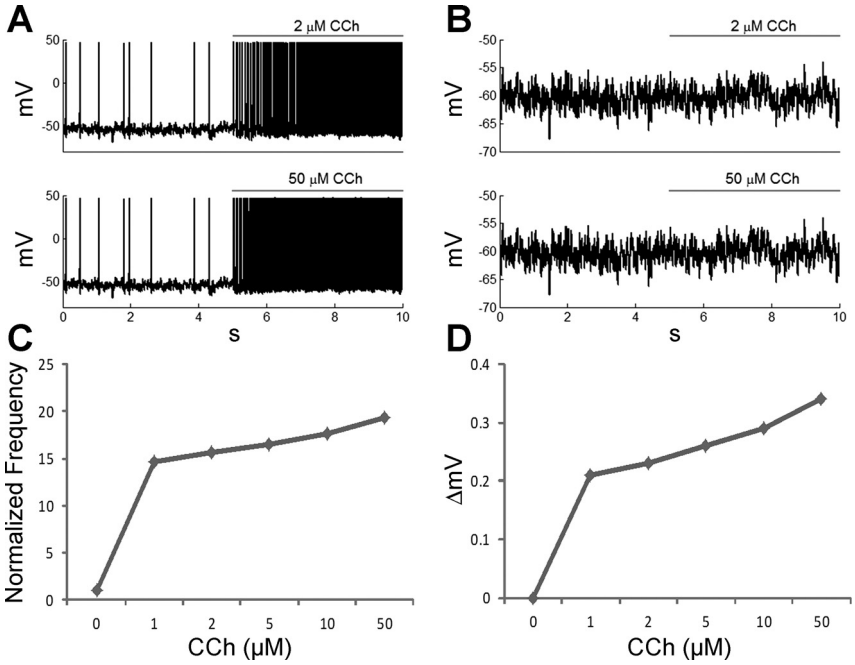

Fig. 4. Effect of CCh on GC spontaneous firing rates and resting membrane potential. *A*: effect of CCh (2.0 and 50.0 μM) on GC spontaneous firing activity. The horizontal bar indicates the duration of neuromodulation. *B*: effect of CCh (2.0 and 50.0 μM) on GC resting membrane potential. For this panel, the amplitude of random background inputs was reduced so that the GC evoked no spontaneous action potentials. *C*: normalized spontaneous firing rates of GCs under different CCh concentrations, including the positive feedback effects of Ca^{2+} accumulation (see text). *D*: changes in the GC resting membrane potential under different CCh concentrations. For this panel, the amplitude of random background inputs was reduced so that the GC evoked no spontaneous action potentials. The effect of CCh on GC resting potential was very weak; note the scale difference on the ordinate compared with the noradrenergic effects depicted in Fig. 5*D*.

why NE modulation had a much larger effect than CCh on the resting membrane potential, we plotted the time courses of the I_M, I_{AHP}, and I_{KL} currents under 0.3 μM and 10.0 μM NE (Fig. 5, *E* and *F*). Before NE application, both the I_M and I_{AHP} currents were largely deactivated at subthreshold potentials, such that blockade of the much larger I_{KL} (with NE) had a much stronger effect on the resting membrane potential than did the blocking of I_M and I_{AHP} (by CCh).

Effects of CCh and NE modulation on GC responses to respiratory input. GCs, like the other cell types of the OB, are subject to slow phasic excitation during respiration (Cang and Isaacson 2003; Pressler et al. 2007). To investigate the effect of CCh and NE modulation on GC responses during respiration, we used a current stimulus composed of trains of α functions (Fig. 6*A*, *bottom*) to simulate the natural excitatory drive onto GCs (Pressler et al. 2007). The prestimulus membrane potential was held at −57 mV to directly reflect experimental data (Fig. 5*A* of Pressler et al. 2007). GC responses to respiratory input (2.5 Hz) under control and 2.0 μM CCh conditions are depicted in Fig. 6*A*. Consistent with experimental data (Fig. 5*A* of Pressler et al. 2007), GC responses partially adapted across trains of four or more respiratory cycles (Fig. 6*A*, *top*) attributable to the progressive activation of I_M and I_{AHP} currents. A comparable adaptation in GC responses was also reported in awake, behaving animals (Cang and Isaacson 2003). Application of 2.0 μM CCh greatly increased the number of APs induced by each respiratory cycle and also transformed the spike frequency adaptation of the control state into spike frequency facilitation; i.e., more spikes were generated by later respiratory cycles than by earlier cycles. Moreover, persistent firing was evoked after the fourth cycle (Fig. 6*A*, *middle*). Figure 6*B* depicts the distribution of spikes across the four cycles (i.e., the percentage of spikes in each cycle relative to the total number of spikes over all 4 cycles) for the control and 2.0 μM CCh cases. Modulation by CCh reversed the direction of cycle-by-cycle change, reducing the proportion of APs evoked by the first respiratory cycle and increasing the proportion of APs evoked by the fourth cycle, owing to progressive Ca^{2+} accumulation and I_{CAN} activation as discussed above, consistent with experimental findings (Fig. 5*A* of Pressler et al. 2007). The average spikes per cycle and average spike latency (averaging across all 4 cycles) then were measured as a function of CCh concentration. The number of spikes per cycle increased sharply with low CCh concentrations, with higher concentrations evoking only modest additional increases (Fig. 6*C*). Latencies to first spike (per cycle) were reduced considerably by low concentrations of CCh (Fig. 6*D*), implying that GC inhibition would likely affect MCs more quickly under cholinergic modulation. To examine the effect of CCh modulation on GC spike distribution within single respiratory cycles, spike-phase distribution plots were generated for control (Fig. 6*E*) and 2.0 μM CCh (Fig. 6*F*) conditions. GC spikes were distributed more broadly with CCh modulation, implying that CCh reduced the phase coupling between GC spikes and respiration. However, the predominant reason for this effect was the large number of additional trailing spikes generated under CCh (Fig. 6*A*); notably, CCh modulation also increased the proportion of spikes in the lowest latency phase bin (0–30°).

The effects of NE modulation on GC responses to respiration-modulated input (Fig. 7*A*, *bottom*) were then assessed. Application of 0.3 μM NE hyperpolarized the prestimulus membrane potential by 4 mV (from −57 mV to −61 mV) and reduced the spikes generated within each cycle (Fig. 7*A*, *upper middle* compared with *top*), whereas application of 3.0 μM NE depolarized the prestimulus membrane potential by 6 mV (from −57 mV to −51 mV) and increased the number of spikes in all cycles (Fig. 7*A*, *lower middle*). However, NE modulation did not eliminate or substantially alter response adaptation, in sharp contrast with CCh neuromodulation (compare Figs. 6*B* and 7*B*). The average numbers of spikes per cycle as a function of NE concentration are depicted in Fig. 7*C*; latencies to first spike (per cycle) as a function of NE concentration are shown in Fig. 7*D*. In contrast to CCh neuromodu-

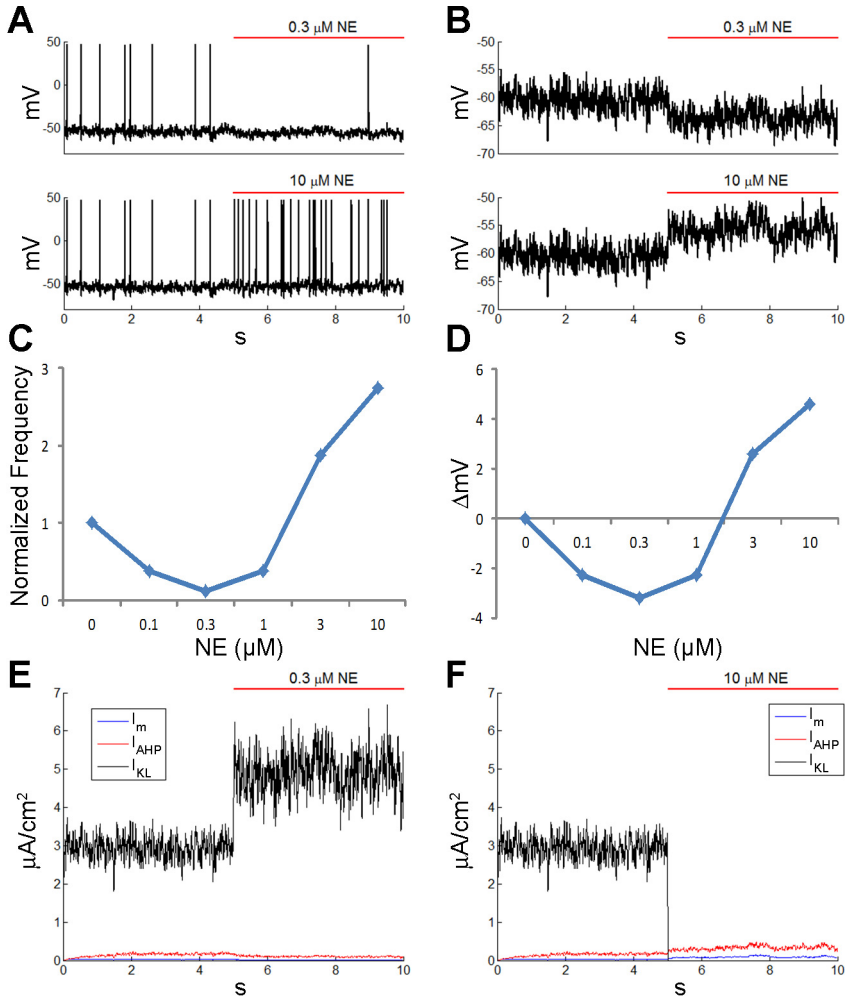

Fig. 5. Effect of NE on GC spontaneous firing rates and resting membrane potential. *A*: effect of NE (0.3 and 10.0 μM) on GC spontaneous firing activity. *B*: effect of NE (0.3 and 10.0 μM) on GC resting membrane potential. For this panel, the amplitude of random background inputs was reduced so that the GC evoked no spontaneous action potentials. *C*: normalized spontaneous firing rates of GCs under different NE concentrations. In addition to being nonmonotonic, this effect was considerably smaller than the CCh effect; note the scale difference on the ordinate compared with Fig. 4*C*. *D*: changes in the GC resting membrane potential under different NE concentrations. For this panel, the amplitude of random background inputs was reduced so that the GC evoked no spontaneous action potentials. *E*: effect on I_M, I_{AHP}, and ohmic potassium (I_{KL}) currents when 0.3 μM NE was applied. *F*: effect on I_M, I_{AHP}, and I_{KL} currents when 10.0 μM NE was applied.

lation, both are nonmonotonic functions of NE concentration, and the spike-rate changes and spike-latency reductions (at higher NE concentrations) were considerably smaller than under CCh (compare Fig. 6, *C* and *D*, with Fig. 7, *C* and *D*).

Interestingly, spike-latency profiles under respiration-patterned stimulation did not always correspond to those under stepped current input. For example, with respiratory stimulation, spike-latency reductions under high NE concentrations (3.0–10.0 μM) were smaller than those under high CCh concentrations (2.0–50.0 μM; compare Figs. 6*D* and 7*D*), but the opposite was true when the neurons were stimulated with single depolarizing current steps (Figs. 1*E* and 2*E*). This difference arose in part because respiratory inputs were applied from more depolarized baselines than were current steps (based on experimental data), at which the I_M and I_{AHP} currents were more activated, but also because spike latencies under respiratory stimulation were measured with respect to all four α functions, such that later cycles under CCh, with their progressively reduced spike latencies owing to progressive Ca^{2+} accumulation and I_{CAN} activation (Fig. 6*A*), contributed to the outcome. The comparative effects of the two modulators therefore can depend on the interactions among multiple state variables, including variables dependent on patterned input and recent activation history.

The GC spike-phase distributions under 0.3 μM and 3.0 μM NE modulation are depicted in Fig. 7, *E* and *F*, respectively (the control state is depicted in Fig. 6*E*). In contrast to CCh modulation (Fig. 6*F*), GC spike phases were distributed much more narrowly under NE modulation, particularly at the lower NE concentration (0.3 μM). That is, NE maintains stronger respiratory coupling of GC spikes than does CCh modulation. Note, however, that these results are predicated on stable concentrations of neuromodulators that (for example) enable steady accumulation of intracellular calcium under CCh neuromodulation. Dynamic regulation of neuromodulator concentrations on (for example) a respiratory time scale could generate quite different results.

Combined effects of CCh and NE modulation on GC afterpotentials and respiratory responses. In vivo, cholinergic and noradrenergic inputs to the OB both are consistently active, such that the two neuromodulators are likely to be present at the same time in the OB circuit. Hence, it is of great interest to investigate how these two neuromodulators interact to shape GC responses to external stimuli. We first looked at the combined effects of CCh and NE modulation on GC afterpotentials. Using the same burst-induction protocol as in Fig. 3, stimulation under control conditions produced a long-lasting AHP (Fig. 8*A*, *top*). Application of 2.0 μM CCh blocked the slow AHP and began to reveal the underlying ADP but did not produce persistent firing (Fig. 8*A*, *middle*). The additional application of 3.0 μM NE depolarized the resting membrane potential by 4 mV (from −60 mV to −56 mV) and generated

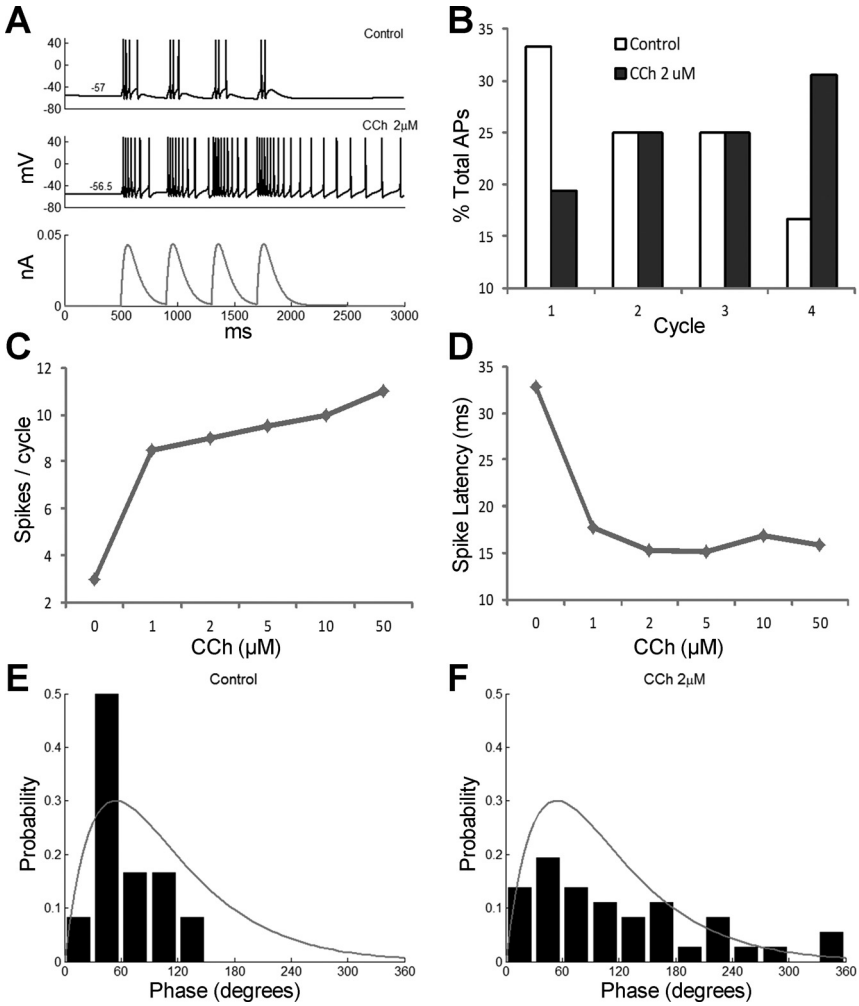

Fig. 6. Effect of CCh on GC responses to 2.5-Hz respiratory input. *A*: GC response to respiratory input under control conditions (*top*) and 2.0 μM CCh (*middle*). A baseline current injection was applied to set a prestimulus membrane potential of -57 mV in the control case; this same current also was applied during CCh modulation. *Bottom*: current stimulus, composed of a 2.5-Hz train of α functions, $\tau = 60$ ms. *B*: percentage of APs in each respiration cycle relative to the total number of APs (in all 4 cycles) under control and CCh conditions. *C*: mean number of spikes per respiration cycle as a function of CCh concentration. *D*: average spike latency (across cycles) as a function of CCh concentration. *E*: spike-phase distribution across the respiratory cycle under control conditions. *F*: spike-phase distribution across the respiratory cycle under 2.0 μM CCh.

persistent firing after burst termination (Fig. 8*A*, *bottom*), comparable to that produced by experimental depolarization under CCh (Fig. 3*C*). A similar effect was observed with respiration-modulated input patterns (Fig. 8*B*). The application of 2.0 μM CCh did not induce persistent firing (when the prestimulus membrane potential remained at -60 mV; Fig. 8*B*, *upper middle*), but the additional application of 3.0 μM NE depolarized the resting membrane potential and generated persistent firing following the fourth respiratory cycle (Fig. 8*B*, *lower middle*). Hence, when the membrane potential is not depolarized by some other process, higher concentrations of NE gate ACh-induced persistent firing in GCs. This is particularly relevant given that GCs in CCh-treated slices rest at around -74 mV and require considerable depolarization to trigger autonomous discharges (Pressler et al. 2007) although the resting potential recorded in vivo is considerably higher (circa -63 mV; Cang and Isaacson 2003).

Although CCh could induce persistent firing in depolarized GCs, the spike-phase distribution was correspondingly broadened (compare Fig. 6, *E* and *F*). Low NE levels (0.3 μM), in contrast, reduced GC excitability and tightened spike-phase distributions (Fig. 7*E*), suggesting that combining CCh with low concentrations of NE could enhance GC responses while maintaining a higher degree of respiratory coupling. Figure 8*C* depicts GC responses to respiratory input under control conditions (Fig. 8*C*, *top*) and under 2.0 μM CCh (Fig. 8*C*, *top middle*), as shown in Fig. 6*A*; Fig. 8*C*, *lower middle* depicts GC responses under a combination of 2.0 μM CCh and a low concentration (0.3 μM) of NE. Notably, GC responses were still enhanced by combined CCh and low-NE modulation (compare Fig. 8*C*, *top* and *lower middle*) although CCh-induced persistent firing was eliminated (compare Fig. 8*C*, *upper middle* and *lower middle*). Additionally, action potentials were now largely constrained within the first half of the respiratory cycle (compare Figs. 6*F* and 8*D*), indicating that NE modulation at low concentrations increased respiratory coupling in the presence of CCh, at the cost of persistent firing.

Effects of CCh and NE modulation on GC responses to high-frequency sniffing input. As noted above, under certain behavioral states, the respiration rate of rodents increases to 4.0–12.0 Hz (e.g., in active, investigative sniffing). Figure 9 depicts the individual and combined effects of CCh and NE modulation on GC responses to high-frequency sniffing input. Sniffing input was modeled as a single aggregate double exponential function based on experimental data, indicating that earlier stages of the olfactory system substantially filter these high-frequency afferent signals (see METHODS). Because of their intrinsic adaptive properties as well as this input attenuation, GCs showed strong frequency adaptation under control conditions (Fig. 9, *top*). In the presence of CCh (2.0 μM), GCs overcame the input attenuation and fired continuously at a stable frequency (Fig. 9*A*, *top*, *middle*). Importantly,

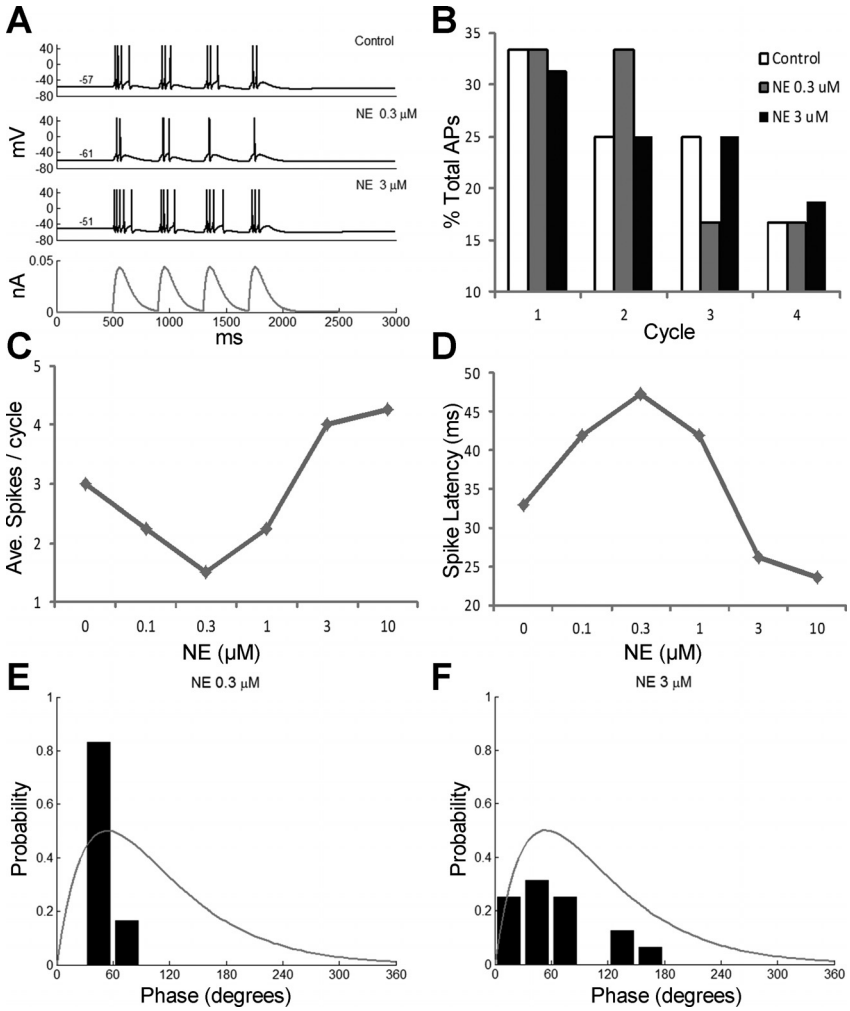

Fig. 7. Effect of NE on GC responses to 2.5-Hz respiratory input. *A*: GC response to a respiratory input under control conditions (top) and 2 concentrations of NE (*upper middle*: 0.3 μM, *lower middle*: 3.0 μM). The same baseline current injection used for the control and CCh simulations (Fig. 6) was applied here; note that NE application alters the resting membrane potential. *Bottom*: current stimulus, composed of a 2.5-Hz train of α functions, $\tau = 60$ ms. *B*: percentage of APs in each respiration cycle relative to the total number of APs (in all 4 cycles) under control, 0.3 μM NE, and 3.0 μM NE conditions. *C*: mean number of spikes per respiration cycle as a function of NE concentration. *D*: average spike latency (across cycles) as a function of NE concentration. *E*: spike-phase distribution across the respiratory cycle under 0.3 μM NE. *F*: spike-phase distribution across the respiratory cycle under 3 μM NE.

CCh modulation induced persistent firing after the termination of sniffing input. Comodulation by 0.3 μM NE maintained the high, nonadapting firing rate response of the GC during sniffing but eliminated persistent firing (Fig. 9*A*, *bottom*, *middle*).

In the absence of CCh modulation, low concentrations of NE (0.3 μM) enhanced frequency adaptation (Fig. 9*B*, *top*, *middle*), whereas high concentrations of NE (3.0 μM) reduced frequency adaptation but did not eliminate it (Fig. 9*B*, *bottom*, *middle*). As with low-frequency respiratory inputs (Fig. 8*B*), 2.0 μM CCh alone was not able to evoke persistent firing in response to high-frequency sniffing inputs if the resting membrane potential was hyperpolarized to -60 mV (Fig. 9*C*, *top*, *middle*). Additional application of high-concentration NE (3.0 μM) depolarized the prestimulus membrane potential to -56 mV, enabling sustained firing after termination of the sniffing input (Fig. 9*C*, *bottom*, *middle*). Overall, the combinatorial effects of CCh and NE modulation on GC responses to higher-frequency sniffing inputs were similar to those presented with lower-frequency respiratory inputs.

Effects of CCh and NE modulation on microcircuit responses to respiratory input. To examine how the neuromodulation of GC responses by CCh and NE impacts the output of MCs (OB principal neurons), we constructed a small microcircuit network consisting of 2 MCs and 30 GCs connected with dendrodendritic reciprocal synapses (both MCs were synaptically connected to all GCs). In this microcircuit, MCs received direct afferent (odor) input and synaptically excited GCs, whereas GCs received afferent input indirectly via MCs and delivered synaptic inhibition onto MCs (see METHODS). Thus, compared with the single-cell simulations described above, GCs received more complex, spike-mediated inputs. Also, whereas the GC response had no effect on its own input in the above simulations, within these microcircuit simulations, GCs delivered feedback inhibition onto MCs, thereby actively shaping their own input. Both MCs and GCs also received random background inputs and fired spontaneously; to simulate network activities in vivo, we adjusted the strength of these background inputs so that MCs fired at a spontaneous rate of ~3.0 Hz, whereas GCs fired at ~0.5 Hz, consistent with in vivo recording data (Cang and Isaacson 2003).

Individual and combined effects of CCh and NE modulation on overall neuronal activity in the microcircuit during respiratory input (2.5 Hz) are shown in Fig. 10; effects on MC spike distribution and synchronization are depicted in Fig. 11. Under control conditions, MCs fired bursts of spikes in each respiratory cycle (Fig. 10*A*; top 2 panels depict the 2 MCs), whereas GCs fired only a few spikes in each cycle owing to spike frequency adaptation (Fig. 10*A*; third and fourth panels depict two typical GCs). The average odor-evoked MC firing rate was 14.8 Hz, much higher than that of GCs (4.4 Hz). With application of 2.0 μM CCh (Fig. 10*B*), the odor-evoked GC firing rate significantly increased (controls: 4.4 Hz; CCh: 11.7 Hz),

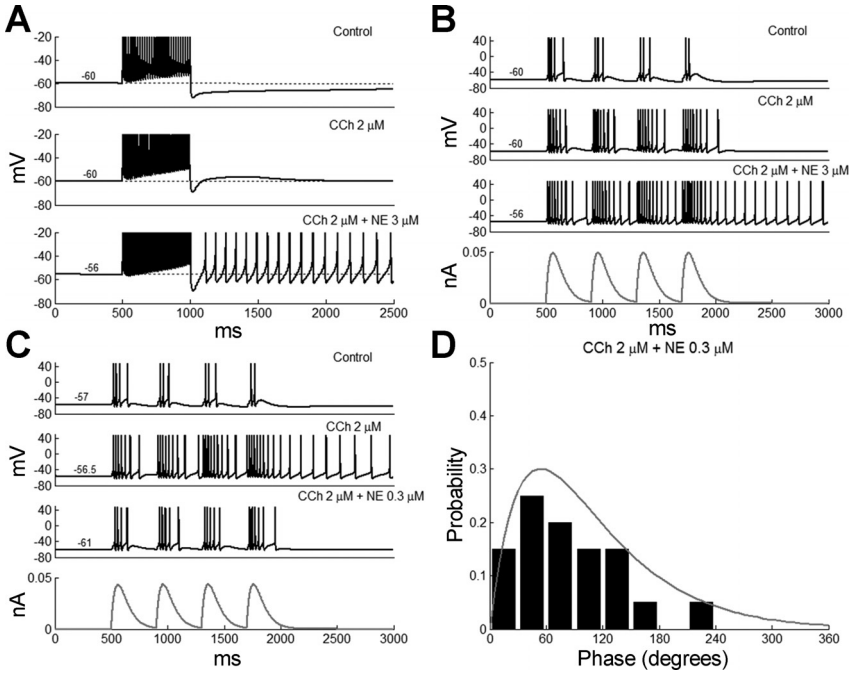

Fig. 8. Combined effect of CCh and NE on GC afterpotentials and responses to respiratory input. *A*: GC burst afterpotential under control conditions (*top*), CCh modulation (2.0 μM, *middle*), and combined CCh (2.0 μM) and NE (3 μM) modulation (*bottom*). The spike burst was induced with a 100-pA, 500-ms current pulse. Note that NE application depolarizes the prestimulus resting potential. *B*: GC responses to respiratory input under control conditions (*top*), CCh modulation (2.0 μM, *upper middle*), and combined CCh (2.0 μM) and NE (3 μM) modulation (*lower middle*). A baseline current injection was applied to set the prestimulus voltage to −60 mV in the control case; this current remained constant in the 2 other cases. *Bottom*: current stimulus, composed of a 2.5-Hz train of α functions, τ = 60 ms. *C*: GC responses to respiratory input under control conditions (*top*), CCh modulation (2.0 μM, *upper middle*), and combined CCh (2.0 μM) and NE (0.3 μM) modulation (*lower middle*). A baseline current injection was applied to set the prestimulus voltage at −57 mV in the control case; this current remained constant in the 2 other cases. *Bottom*: current stimulus, composed of a 2.5-Hz train of α functions, τ = 60 ms. *D*: spike-phase distribution across the respiratory cycle under combined CCh (2.0 μM) and NE (0.3 μM) modulation.

reducing the MC firing rate during odor presentation (controls: 14.8 Hz; CCh: 12.3 Hz). This inhibitory effect was most pronounced in later respiratory cycles because of the progressive CCh-dependent activation of the depolarizing I_{CAN} current in GCs. After odor presentation, the GC spontaneous activities were substantially increased compared with controls (attributable to ADP), suppressing MC spontaneous activities (spontaneous rate after odor presentation: controls: 3.0 Hz, CCh: 1.5 Hz; compare Fig. 10, *A* and *B*). Higher CCh concentrations further reduced MC spontaneous activities after odor input (results not shown). In addition to MC firing-rate suppression, CCh application substantially enhanced MC spike synchrony (SI) (controls: 0.31; CCh: 0.47; compare Fig. 11*A*, *top* and *bottom*). Moreover, the distributions of MC spikes across each respiratory cycle were altered by CCh application. Under CCh (2.0 μM) modulation, the proportion of MC spikes in the earliest phase bin was reduced, whereas spiking during the crest of the respiration was increased (compare Fig. 11*B*, *top* and *bottom*). Also, the MC spikes in the latest phase bin (330–360°) were eliminated because of sustained GC depolarization. The overall effect was a slight increase of spike coupling with the respiratory cycles (respiration coupling index) (controls: 0.60; CCh: 0.64).

With application of a low concentration of NE (0.3 μM), the GC membrane potential was hyperpolarized, yielding higher spontaneous activity levels in MCs (Fig. 10*C*). During odor presentations, odor-evoked GC firing rates were reduced below control rates (controls: 4.4 Hz; NE 0.3 μM: 1.9 Hz), whereas odor-evoked MC firing rates were essentially unchanged (controls: 14.8 Hz; NE 0.3 μM: 15.0 Hz). MC spike synchrony was unchanged or slightly reduced by 0.3 μM NE application (SI, controls: 0.31; NE 0.3 μM: 0.29; compare Fig. 11*A*, *top*, with Fig. 11*C*, *top*). In contrast, when a higher concentration of NE (3.0 μM) was applied, the baseline GC membrane potential

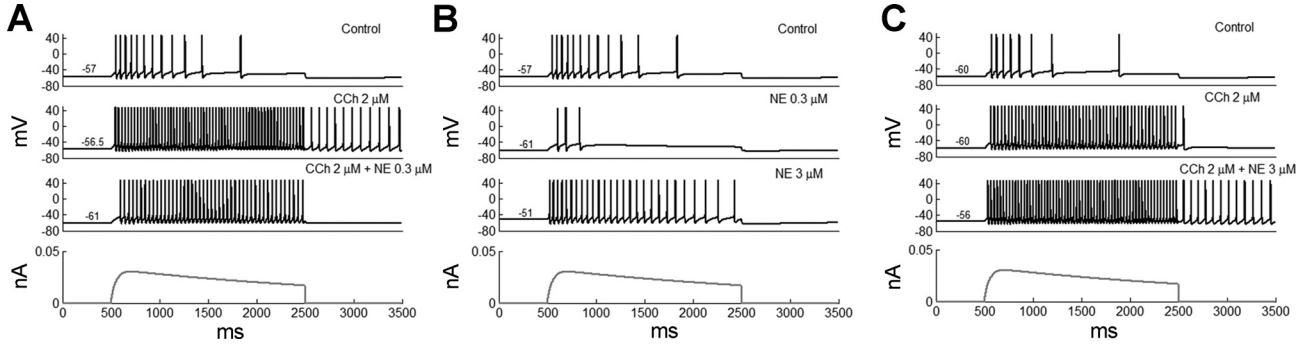

Fig. 9. Effect of CCh and NE on GC response to filtered high-frequency sniffing input. *A*: GC response to sniffing input under control conditions (*top*), CCh modulation (2.0 μM, *upper middle*), and combined CCh (2.0 μM) and NE (0.3 μM) modulation (*lower middle*). *Bottom*: filtered envelope of high-frequency sniffing input modeled by a double exponential function with τ_1 = 50 ms and τ_2 = 3,000 ms. *B*: GC responses to sniffing input under control conditions (*top*), and 2 levels of NE modulation (*upper middle*: 0.3 μM; *lower middle*: 3.0 μM). *Bottom*: filtered envelope of high-frequency sniffing input modeled by a double exponential function with τ_1 = 50 ms and τ_2 = 3,000 ms. For *A* and *B*, a baseline current injection was applied to set the prestimulus voltage to −57 mV in the control case; this current remained constant in the other (modulated) cases. *C*: GC responses to sniffing input under control (*top*), CCh modulation (2.0 μM, *upper middle*), and combined CCh (2.0 μM) and NE (3.0 μM) modulation (*lower middle*). A baseline current injection was applied to set the prestimulus voltage to −60 mV in the control case; this current remained constant in the 2 other cases. *Bottom*: filtered envelope of high-frequency sniffing input modeled by a double exponential function with τ_1 = 50 ms and τ_2 = 3,000 ms.

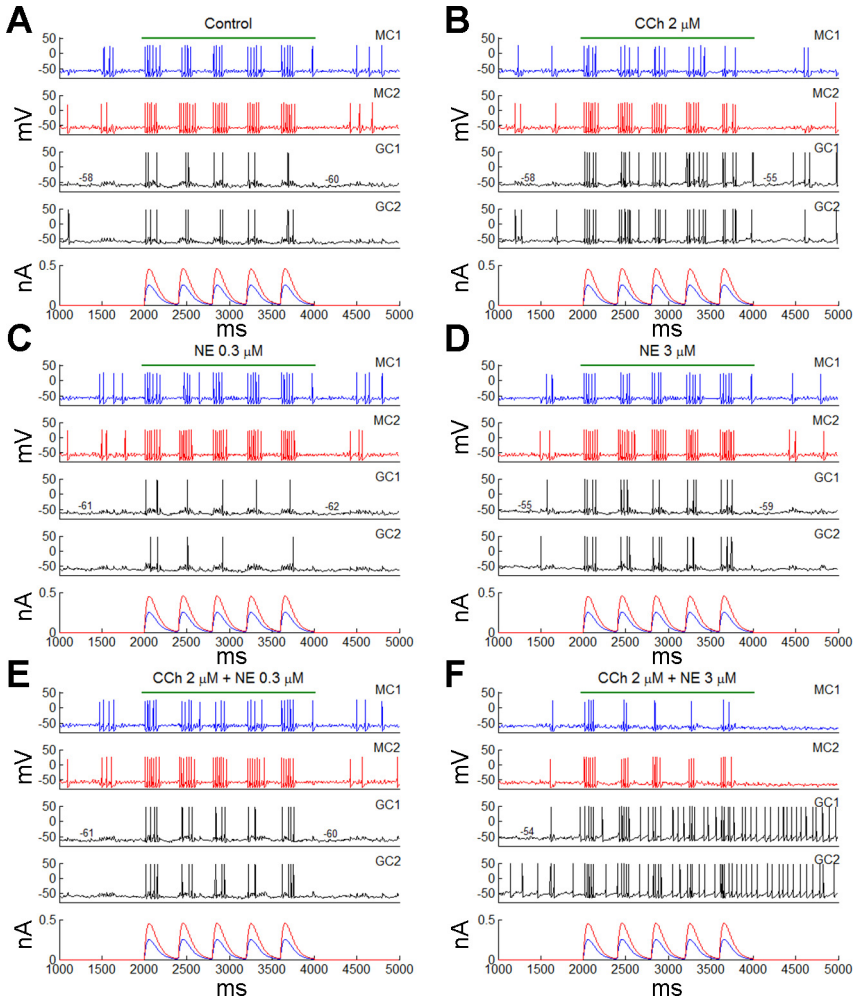

Fig. 10. Separate and combined effects of CCh and NE on neuronal activity in the mitral cell (MC)-GC microcircuit network, in response to 2.5-Hz respiratory input delivered to the MCs. All figures depict the responses of both MCs and 2 of the 30 GCs (*top 4 panels*) to respiratory inputs (*bottom*) under the following 6 conditions: control conditions (*A*), CCh (2.0 μM) modulation (*B*), low-NE (0.3 μM) modulation (*C*), high-NE (3.0 μM) modulation (*D*), combined CCh (2.0 μM) and low-NE (0.3 μM) modulation (*E*), combined CCh (2.0 μM) and high-NE (3.0 μM) modulation (*F*). The green bars indicate the duration of odor input, and the numbers above the first GC voltage trace indicate the baseline GC membrane potential measured before and after the odor-stimulus period.

was depolarized (from −58 mV in controls to −55 mV, Fig. 10*D*), reducing the spontaneous MC spike rate from ~3.0 Hz to ~2.0 Hz. During odor stimulation, 3.0 μM NE increased odor-evoked GC firing rate slightly (controls: 4.4 Hz; NE 3.0 μM: 6.6 Hz) but had no effect on the odor-evoked MC firing rate (controls: 14.8 Hz; NE 3.0 μM: 14.8 Hz; compare Fig. 10, *A* and *D*). Consequently, in agreement with experimental data, higher concentrations of NE inhibited spontaneous, but not odor-evoked, MC firing, thereby increasing the SNR of odor activation in MCs (Linster et al. 2011). Whereas NE (0.3 μM) slightly reduced MC synchrony, NE (3.0 μM) increased MC spike synchronization, but to a lesser degree than 2.0 μM CCh (SI, controls: 0.31; CCh 2.0 μM: 0.47; NE 0.3 μM: 0.29; NE 3.0 μM: 0.40; compare Fig. 11, *A* and *C*). The MC phase distribution plots under both concentrations of NE are shown in Fig. 11*D*. The respiration coupling index indicated that 0.3 μM NE minimally reduced, whereas 3.0 μM NE slightly increased, the respiratory phase locking of MC spiking activity (controls: 0.60, NE 0.3 μM: 0.57; NE 3.0 μM: 0.66).

When 2.0 μM CCh was applied together with the lower concentration of NE (0.3 μM), the baseline GC membrane potential was hyperpolarized (from around −58 mV in controls to around −61 mV; compare Fig. 10, *A* and *E*), and the MC spontaneous firing rate increased (from ~3.0–~4.0 Hz), similar to the effects of NE application alone. However, the gradually depolarizing effect of CCh modulation across odor presentations (Fig. 10*B*) was eliminated by additional NE application, such that the GC membrane potential remained stable during and after odorant presentations (Fig. 10*E*) and the CCh-induced reduction in MC spontaneous activity following odor presentations was removed (compare the top 2 panels of Fig. 10, *B* and *E*). Because the excitatory CCh effect overcame the inhibitory NE effect, the odor-evoked GC firing rate was slightly increased from 4.4 Hz (in controls) to 6.9 Hz, but the odor-evoked MC firing rate was essentially unchanged (controls: 14.8 Hz; CCh 2.0 μM + NE 0.3 μM: 14.3 Hz). Spike synchronization between the two MCs increased but to a lesser degree than under CCh alone (SI, controls: 0.31; CCh 2.0 μM: 0.47; CCh 2.0 μM + NE 0.3 μM: 0.36; compare the top panels of Fig. 11, *A* and *E*). The MC spike-phase distribution under simultaneous CCh and NE (0.3 μM) modulation is shown in Fig. 11*F*, *top*. Compared with controls or separate CCh or NE modulation, combined CCh and low-concentration NE (0.3 μM) modulation induced a higher proportion of spikes in the second half (180–360°) of the respiration cycle (compare Fig. 11, *B* and *D*, with Fig. 11*F*, *top*). As a result, the respiration coupling index was slightly reduced (controls: 0.60; CCh 2.0 μM: 0.64; NE 0.3 μM: 0.57; CCh 2.0 μM + NE 0.3 μM: 0.53). In contrast, the simultaneous application of CCh (2.0 μM) and high-concentration NE (3.0 μM) imposed a strong inhibitory effect on MCs by substantially potentiating GC excitability (Fig. 10*F*). Both the membrane potentials and

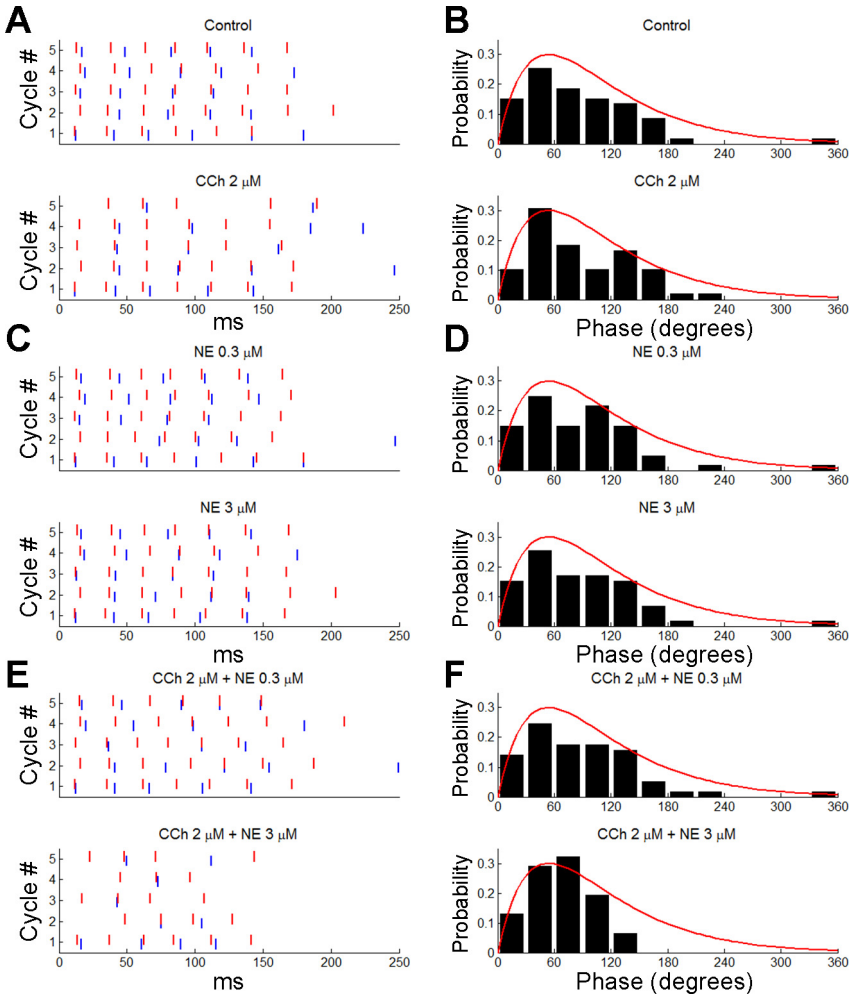

Fig. 11. Separate and combined effects of CCh and NE on MC spike synchronization and distribution across respiratory cycles in the MC-GC microcircuit network. *A*: spike raster plots of the 2 MCs in the microcircuit (blue: MC1; red: MC2) across 5 respiratory cycles under control conditions (*top*) and CCh (2.0 μM) modulation (*bottom*). Spiking activity is depicted for only the first 250 ms of each 400-ms respiration cycle. *B*: spike-phase distribution of both MCs across 5 respiratory cycles under control conditions (*top*) and CCh (2.0 μM) modulation (*bottom*). The overlay of α function depicts the respiratory waveform. *C*: as in *A*, but with low-NE (0.3 μM) modulation (*top*) and high-NE (3.0 μM) modulation (*bottom*). *D*: as in *B*, but with low-NE (0.3 μM) modulation (*top*) and high-NE (3.0 μM) modulation (*bottom*). *E*: as in *A*, but with combined CCh (2.0 μM) and low-NE (0.3 μM) modulation (*top*) and combined CCh (2.0 μM) and high-NE (3.0 μM) modulation (*bottom*). *F*: as in *B*, but with combined CCh (2.0 μM) and low-NE (0.3 μM) modulation (*top*) and combined CCh (2.0 μM) and high-NE (3 μM) modulation (*bottom*).

spontaneous firing rates of GCs before and after odor presentation were significantly affected, yielding a substantial reduction of baseline MC spontaneous activity and a complete suppression of MC activity after odor presentation (compare Fig. 10, *A* and *F*). The odor-evoked GC firing rate increased almost fourfold (controls: 4.4 Hz; CCh 2.0 μM + NE 3.0 μM: 16.2 Hz), with GCs firing even in the absence of MC inputs (Fig. 10*F*). Consequently, the odor-evoked MC firing rate was substantially reduced (controls: 14.8 Hz; CCh 2.0 μM + NE 3.0 μM: 7.8 Hz). The MC spikes also showed a high degree of synchronization (Fig. 11*E*, *bottom*), slightly less than that of CCh application alone but substantially higher than under control conditions (SI, controls: 0.31; CCh 2.0 μM: 0.47; CCh 2.0 μM + NE 3.0 μM: 0.42). Moreover, MC spikes were well constrained within the early phase of the respiratory cycles (i.e., all spikes fell within 0–150°), indicating a substantial enhancement of phase locking between MC spikes and respiration (compare Fig. 11*B*, *top*, with Fig. 11*F*, *bottom*). Consequently, the respiration coupling index was the largest among all six conditions simulated (controls: 0.60; CCh 2.0 μM: 0.64; NE 0.3 μM: 0.57; NE 3.0 μM: 0.66; CCh 2.0 μM + NE 0.3 μM: 0.53; CCh 2.0 μM + NE 3.0 μM: 0.84).

The summarized effects of CCh and NE modulation on odor-evoked MC/GC firing rates, neuronal SNRs, MC spike latencies, and MC spike synchronization indices in the microcircuit model across a range of simulated concentrations are depicted in Fig. 12. Each plot is an average of results from 10 microcircuit simulations, each initiated with a different random seed. As CCh concentration increased, GC firing rates increased rapidly, causing a corresponding reduction in MC firing rates (Fig. 12*A*), whereas the effects of NE on GC and MC odor-evoked firing rates were much weaker (Fig. 12*B*). Notably, even 50.0 μM CCh did not promote depolarization block in GCs in the microcircuit model, in contrast to main OB slice studies (Pressler et al. 2007) and cellular GC simulations (Fig. 1*F*). This contrast arose because GCs in the microcircuit model are excited by dendritic synaptic inputs from spiking MCs rather than by strong, continuous somatic current injection. This result highlights the importance of contrasting such common in vitro vs. in vivo experimental approaches when interpreting the physiological effects of experimental manipulations.

Increased CCh concentrations also marginally reduced the sensory SNR in MCs (the ratio of the odor-evoked firing rate to the prestimulus spontaneous firing rate; Fig. 12*C*), largely because CCh suppressed odor-evoked MC firing rates more sharply than it did spontaneous firing. Under NE modulation, the SNR was affected more by modulation of the spontaneous firing rate. As NE in low concentrations (0.1–1.0 μM) increased spontaneous firing rates, whereas higher concentrations (3.0–10.0 μM) reduced spontaneous firing in MCs, lower

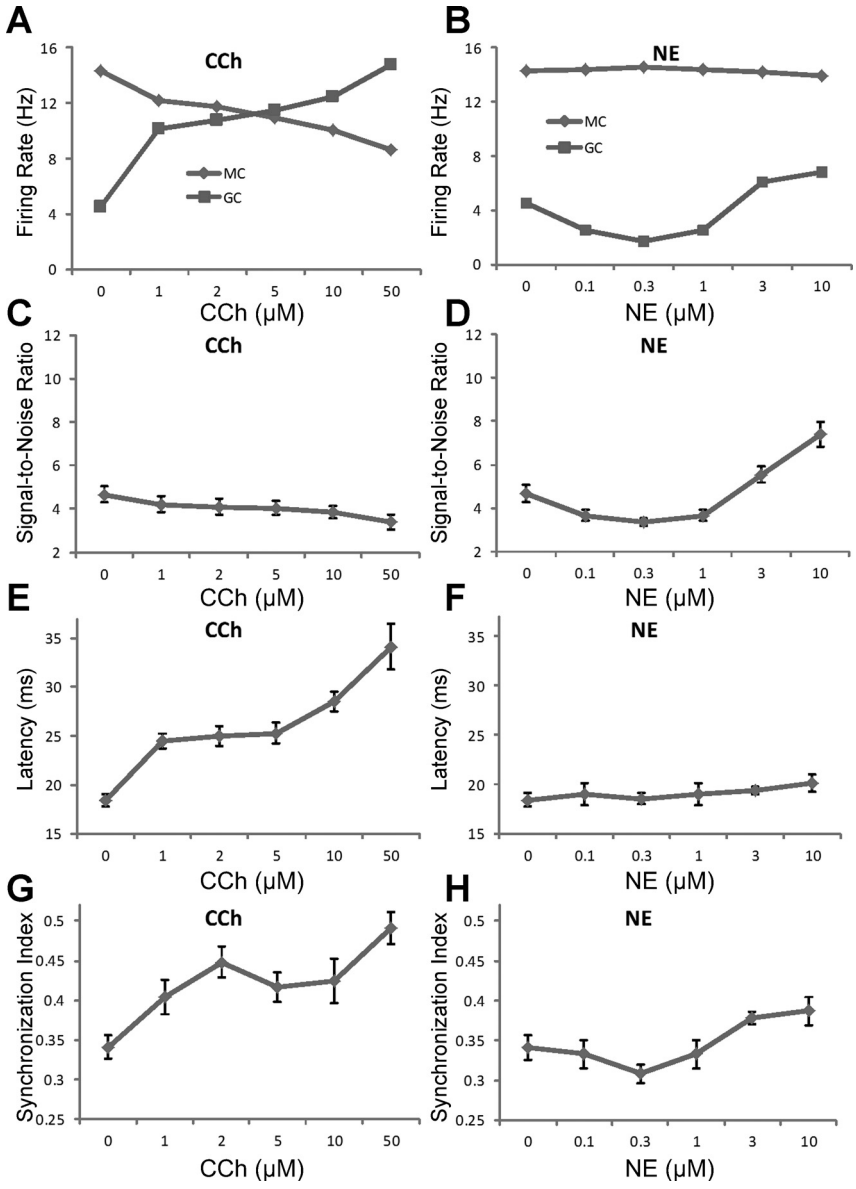

Fig. 12. Effects of CCh and NE on MC and GC firing rates, signal-to-noise ratios, MC spiking latency, and spike synchrony in the MC-GC microcircuit network, in response to 2.5-Hz respiratory input. *A*: odor-evoked MC and GC firing rates at different concentrations of CCh. *B*: odor-evoked MC and GC firing rates at different concentrations of NE. Firing rates are averages over all phases of 5 respiratory cycles. *C*: signal-to-noise ratios in MCs at different concentrations of CCh. *D*: signal-to-noise ratios in MCs at different concentrations of NE. The signal-to-noise ratio of a neuron was defined as the ratio of the odor-evoked MC firing rate to the prestimulus spontaneous firing rate. *E*: latency to first spike (per cycle) following odor stimulation at different concentrations of CCh. *F*: latency to first spike (per cycle) following odor stimulation at different concentrations of NE. *G*: MC spike synchronization index at different concentrations of CCh. *H*: MC spike synchronization index at different concentrations of NE. All panels depict averaged results from 10 microcircuit network simulations, each initiated with a different random seed. Error bars denote the standard error of the mean (error is too small to see in *A* and *B*).

concentrations of NE reduced the SNR, whereas higher NE concentrations substantially improved the SNR (Fig. 12*D*).

The latency to first spike in MCs following afferent stimulation was substantially affected by cholinergic neuromodulation. Increasing concentrations of CCh progressively delayed the onset of MC spiking (Fig. 12*E*) owing to the strong and extended synaptic inhibition received from GCs. In contrast, MC spike latencies were relatively unaffected by NE modulation (Fig. 12*F*). Finally, consistent with previous simulation studies (Li and Cleland 2013), cholinergic neuromodulation exerted a strong synchronizing effect on MC spikes by potentiating GC-mediated synaptic inhibition. As the CCh concentration increased, the SI increased rapidly to a peak at ~2.0 μM, then slightly declined at concentrations around 5.0 μM before increasing again at higher concentrations (Fig. 12*G*). In contrast, the synchronizing effect of NE modulation on MC spikes was much weaker, with a slight enhancement at higher concentrations of NE (3.0–10.0 μM; Fig. 12*H*). The stronger effect of CCh arose largely because of the increased odor-evoked firing rates and extended postspike ADPs in GCs, which provided strong phasic synaptic inhibition onto MCs.

To compare the separate CCh and NE modulatory effects on microcircuit activity with their combinatorial effects, we plotted the same four physiological activity metrics (odor-evoked MC/GC firing rates, MC SNR, MC spike latency, and MC spike SI) under six modulatory conditions (control, CCh 2.0 μM, NE 0.3 μM, NE 3.0 μM, CCh 2.0 μM + NE 0.3 μM, CCh 2.0 μM + NE 3.0 μM) in Fig. 13. As noted above, MC firing rates were relatively stable under NE modulation and under combined CCh and low-concentration NE (0.3 μM) modulation but were slightly reduced under CCh modulation and strongly suppressed under combined CCh and high-concentration NE (3.0 μM; Fig. 13*A*). GC firing rates increased under CCh and changed nonmonotonically under increasing NE concentrations, also as described above; the combinatorial effects of these modulators on GC firing rates appeared straightforward (Fig. 13*A*). The neuronal SNR of MCs was slightly reduced under CCh, NE 0.3

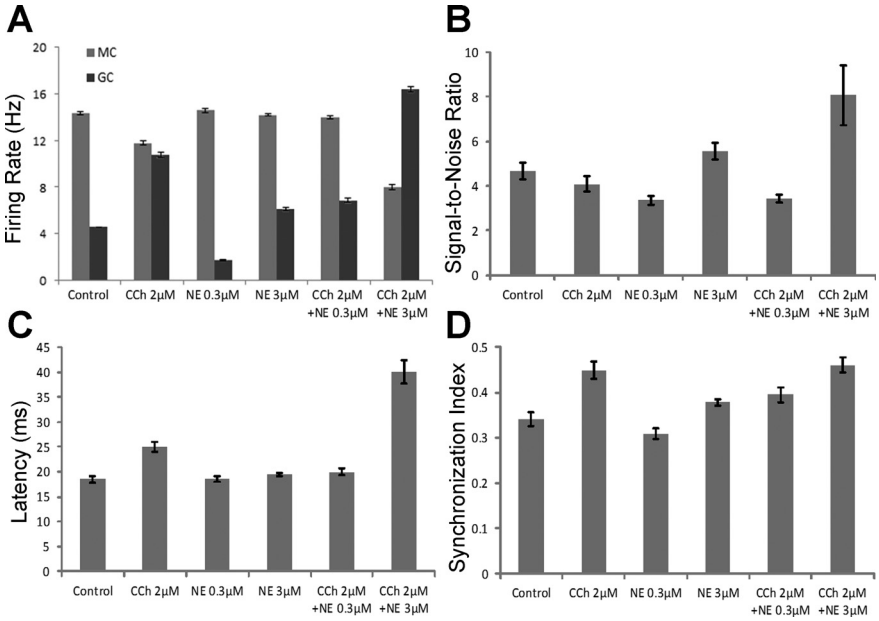

Fig. 13. Comparison of the effects of separate and combined CCh and NE neuromodulation on MC-GC microcircuit response properties in response to 2.5-Hz respiratory input. *A*: effects on MC and GC firing rates. *B*: effects on MC signal-to-noise ratios. *C*: effects on MC spike latency. *D*: effects on MC spike synchrony. All panels depict averaged results from 10 microcircuit network simulations, each initiated with a different random seed. Error bars denote the standard error of the mean.

μM, and their combination but was moderately increased under NE 3.0 μM modulation and supralinearly enhanced under combined CCh and NE 3.0 μM modulation; that is, CCh reduced the SNR on its own but potentiated the increased SNR evoked by 3.0 μM NE (Fig. 13*B*). The MC spike latency remained relatively unchanged under NE modulation (both 0.3 μM and 3.0 μM) and combined CCh and low-concentration NE (0.3 μM) modulation but was modestly increased under CCh modulation and substantially increased under combined CCh and high-concentration NE (3.0 μM; Fig. 13*C*). Lastly, the MC spike SI was slightly reduced under low-concentration NE (0.3 μM) and slightly increased under high-concentration NE (3.0 μM). By comparison, the SI was substantially enhanced by CCh modulation, particularly in combination with high-concentration NE (3.0 μM). Overall, the degree of MC synchrony reflected the strength of phasic inhibition from GCs, as MC spikes were more tightly constrained by stronger GC inhibition.

Effects of CCh and NE modulation on microcircuit responses to sniffing input. We next investigated the effect of CCh and NE modulation on microcircuit activity corresponding to active odorant sampling (i.e., based on the quasitonic afferent input arising from high-frequency sniffing behavior). Afferent stimulation was delivered to the two MCs of the microcircuit with the same time course but at slightly different amplitudes to reflect the nonuniform input activation patterns of natural odorants (Fig. 14, *bottom*). Under control conditions, both GCs and MCs showed adaptation as afferent input strength slowly decayed (Fig. 14*A*). Because of the tonic nature of the filtered sniffing input, the odor-evoked mean firing rate of MCs (23.3 Hz) was considerably higher than that measured in response to low-frequency respiratory input (14.8 Hz; compare Figs. 10*A* and 14*A*). Application of CCh (2.0 μM) greatly increased the odor-evoked GC firing rate (controls: 5.9 Hz; CCh 2.0 μM: 19.3 Hz), resulting in a considerable reduction of the odor-evoked MC firing rate (controls: 23.3 Hz; CCh 2.0 μM: 16.5 Hz; Fig. 14*B*). The firing-rate suppression was stronger on the MC receiving the weaker afferent input (i.e., MC1; compare Fig. 14, *A* and *B*). As observed with the slower, periodic respiratory input, CCh inhibited poststimulus MC spontaneous activity more than prestimulus activity because of the ADP currents and sustained firing arising in GCs after odor presentation (Fig. 14*B*). MC spike synchrony during odor presentation also was enhanced with CCh modulation (SI, controls: 0.33; CCh 2.0 μM: 0.40).

When a low concentration of NE (0.3 μM) was applied, GCs showed stronger frequency adaptation with lower odor-evoked firing rates (controls: 5.9 Hz; NE 0.3 μM: 2.6 Hz), whereas the firing rate of MCs remained unaffected (controls: 23.3 Hz; NE 0.3 μM: 23.5 Hz; Fig. 14*C*). MC spike synchrony was unaffected or very slightly reduced by application of 0.3 μM NE (SI, controls: 0.33; NE 0.3 μM: 0.31). A higher concentration of NE (3.0 μM), in contrast, moderately increased the odor-evoked GC firing rate (controls: 5.9 Hz; NE 3.0 μM: 9.2 Hz) while leaving the MC firing rate unchanged (controls: 23.3 Hz; NE 3.0 μM: 23.3 Hz; Fig. 14*D*). Overall, during active odor sampling (sniffing), the MC firing rate was relatively insensitive to moderate changes in GC firing rate. As observed under slower respiratory inputs, NE at high concentration (3.0 μM) suppressed prestimulus MC spontaneous activity more than poststimulus activity (compare Fig. 14, *A* and *D*) and slightly increased MC spike synchronization (SI, controls: 0.33; NE 3.0 μM: 0.37).

Coapplication of CCh (2.0 μM) and low-concentration NE (0.3 μM) significantly increased odor-evoked GC firing rates although to a lesser degree than CCh application alone (controls: 5.9 Hz; CCh 2.0 μM: 19.3 Hz; CCh 2.0 μM + NE 0.3 μM: 14.9 Hz; Fig. 14*E*). However, the odor-evoked MC firing rate was only slightly reduced compared with controls (controls: 23.3 Hz; CCh 2.0 μM: 16.5 Hz; CCh 2.0 μM + NE 0.3 μM: 22.0 Hz), again indicating that MC firing rates during sniffing were relatively insensitive to GC firing rate changes. As 0.3 μM NE hyperpolarized the GCs and eliminated persistent firing, it also reduced the poststimulus inhibition on MCs induced by CCh application (compare Fig. 14, *B* and *E*). The addition of 0.3 μM NE did not reduce MC spike synchrony in this case (SI, controls: 0.33; CCh 2.0 μM: 0.4; CCh 2.0 μM +

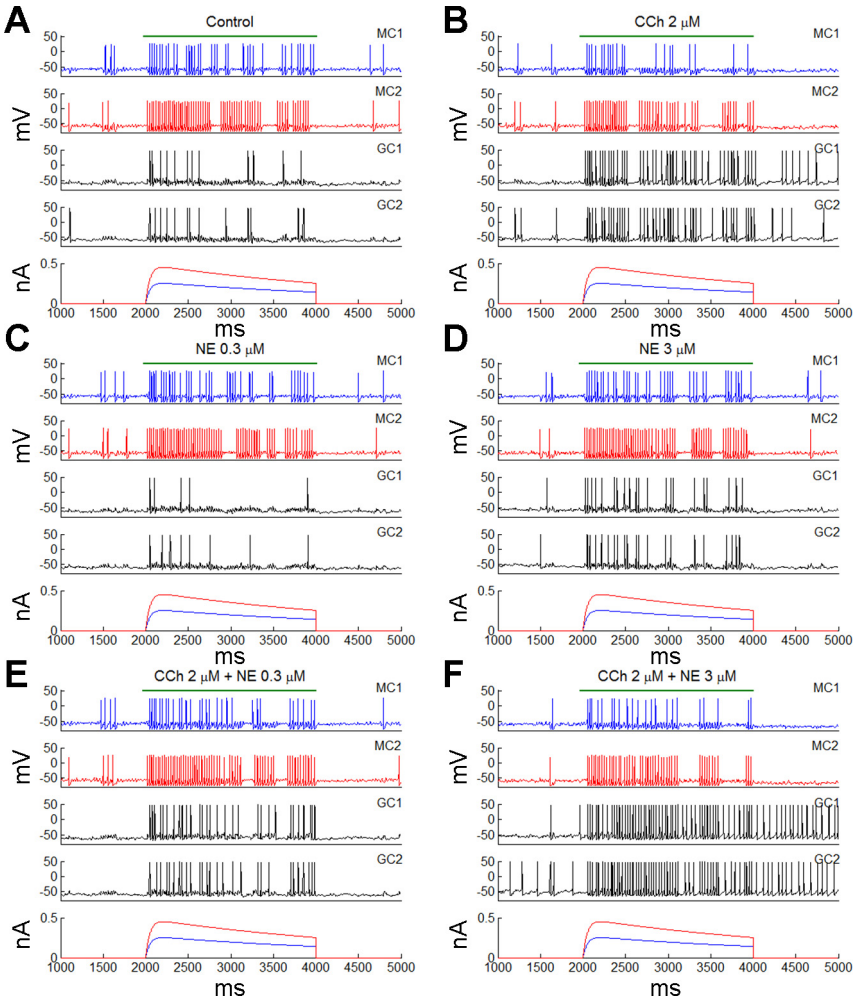

Fig. 14. Separate and combined effects of CCh and NE on neuronal activity in the MC-GC microcircuit network, in response to filtered high-frequency sniffing input delivered to the MCs. The envelope of this sniffing input was modeled by a double exponential function with $\tau_1 = 50$ ms and $\tau_2 = 3{,}000$ ms. All panels depict the responses of both MCs and 2 of the 30 GCs (*top 4 panels*) in response to sniffing input (*bottom*) under the following 6 conditions: control conditions (*A*), CCh (2.0 μM) modulation (*B*), low-NE (0.3 μM) modulation (*C*), high-NE (3.0 μM) modulation (*D*), combined CCh (2.0 μM) and low-NE (0.3 μM) modulation (*E*), combined CCh (2.0 μM) and high-NE (3.0 μM) modulation (*F*). Green bars indicate the duration of odor input.

NE 0.3 μM: 0.41), largely because the GC firing rate (i.e., phasic inhibition) was still high.

Simultaneous application of CCh (2.0 μM) and the higher concentration of NE (3.0 μM) suppressed MC spontaneous activity both before and after odor presentation (Fig. 14*F*), as was also observed with periodic respiratory input (Fig. 10*F*). GCs showed strong persistent firing, and the odor-evoked GC firing rate was much higher than under control conditions (controls: 5.9 Hz; CCh 2.0 μM + NE 3.0 μM: 26.0 Hz), which moderately reduced the odor-evoked MC firing rate (controls: 23.3 Hz; CCh 2.0 μM + NE 3.0 μM: 17.3 Hz). MC spike synchronization was higher than under control conditions or CCh modulation alone (controls: 0.33; CCh 2.0 μM: 0.40; CCh 2.0 μM + NE 3.0 μM: 0.44).

The impact of CCh and NE modulation at a range of different concentrations on odor-evoked responses to (filtered) high-frequency sniffing input is summarized in Fig. 15. Each plot is an average of results from 10 microcircuit simulations, each initiated with a different random seed. As with slow respiratory modulation, increased CCh concentrations sharply increased odor-evoked GC firing rates and correspondingly reduced MC firing rates (Fig. 15*A*), whereas increased NE concentrations had substantially weaker effects on evoked spike rates (Fig. 15*B*). In comparison, the effect of CCh on the response SNR in MCs was minimal (Fig. 15*C*), whereas NE neuromodulation strongly increased the SNR at higher concentrations (Fig. 15*D*). MC spike latencies were calculated differently for high-frequency sniffing input than they were for respiratory input; during slow respiration, spike latencies were averaged across all respiratory cycles (Fig. 12, *E* and *F*), whereas, in the high-frequency sniffing condition, spike latencies were calculated with respect to odor onset only. The effects of CCh were marginal, in contrast to their substantial effects under slow respiration (compare Figs. 12*E* and 15*E*), in large part because the later cycles that followed GC activation contributed substantially to the effect under slow respiration. The effects of NE on spike latency fluctuated across concentrations but were generally weak and sensitive to noise (i.e., larger error bars; Fig. 15*F*). Finally, neuromodulator effects on MC spike synchronization largely tracked the effects under slow respiration, with a substantial and systematic synchronizing effect of increased CCh even at low concentrations (Fig. 15*G*) and a weaker effect of NE observable only at the highest concentrations examined (Fig. 15*H*).

To compare the separate CCh and NE modulatory effects on microcircuit activity with their combinatorial effects, we again plotted the same four physiological activity metrics under the same six modulatory conditions (Fig. 16). Overall, both the separate and combined modulatory effects of CCh and NE on filtered sniffing input were similar to those observed in response to slow, phasic respiratory input (compare Figs. 13 and 16). These results make clear that, whether afferent odor

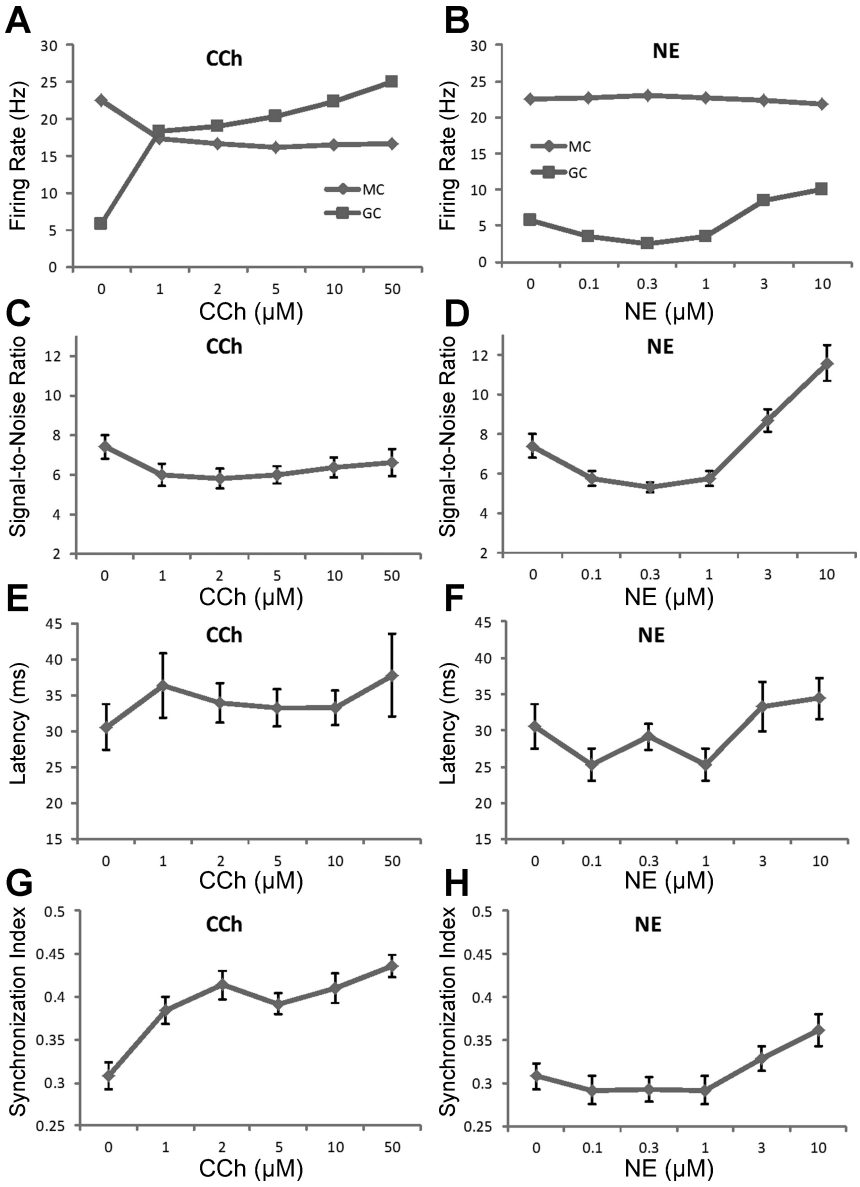

Fig. 15. Effects of CCh and NE on MC and GC firing rates, signal-to-noise ratios, MC spiking latency, and spike synchrony in the MC-GC microcircuit network, in response to filtered high frequency sniffing input. *A*: odor-evoked MC and GC firing rates at different concentrations of CCh. *B*: odor-evoked MC and GC firing rates at different concentrations of NE. *C*: signal-to-noise ratios in MCs at different concentrations of CCh. *D*: signal-to-noise ratios in MCs at different concentrations of NE. The signal-to-noise ratio of a neuron was defined as the ratio of the odor-evoked MC firing rate to the prestimulus spontaneous firing rate. *E*: latency to first spike following odor stimulation at different concentrations of CCh. *F*: latency to first spike following odor stimulation at different concentrations of NE. *G*: MC spike synchronization index at different concentrations of CCh. *H*: MC spike synchronization index at different concentrations of NE. All panels depict averaged results from 10 microcircuit network simulations, each initiated with a different random seed. Error bars denote the standard error of the mean (error is too small to see in *A* and *B*).

signals are periodic or highly filtered, cholinergic neuromodulation is predominantly important for MC spike synchronization, whereas higher concentrations of NE improve the neuronal SNR. Notably, the combinatorial effect of CCh and higher-concentration NE further enhances this SNR although CCh alone exhibits no such effect.

DISCUSSION

One striking feature of the olfactory system is the large amount of centrifugal influence on odor processing in the early olfactory pathways (Fletcher and Chen 2010; Mandairon and Linster 2009). The mammalian OB receives massive cholinergic inputs from the basal forebrain and dense noradrenergic innervations from the locus coeruleus, both of which have profound effects on odor processing as well as on olfactory learning and memory (Devore and Linster 2012; Linster et al. 2011). One common target of cholinergic and noradrenergic modulation is the GC population. GCs are the largest population of inhibitory interneurons in the OB, forming numerous dendrodendritic connections with the secondary (lateral) dendrites of MCs in the OB EPL. By regulating GC excitability, ACh and NE influence MC output and the information that MCs convey to higher cortical structures. Although ACh and NE share some similar effects on GC excitability, they differ in the particular membrane channels that are affected as well as in their specific effects on neuronal response properties. It remains unclear how the modulation of GC intrinsic properties by ACh and NE, and by both together, shapes MC output and gives rise to particular perceptual and behavioral outcomes. Here, we used a biophysical modeling approach to study the individual and combined effects of ACh and NE modulation on the cellular responses of GCs in detail and also how this neuromodulation in GCs affects MC response properties in an EPL synaptic microcircuit. This study, closely constrained by experimental data, provides a systematic understanding of the common and distinct effects of ACh and NE modulation in olfactory sensory processing.

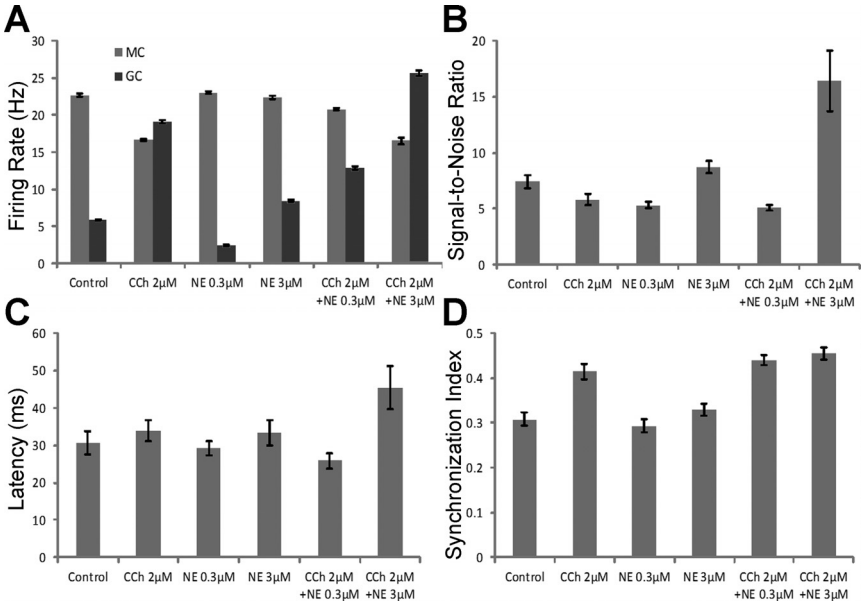

Fig. 16. Comparison of the effects of separate and combined CCh and NE neuromodulation on MC-GC microcircuit response properties in response to filtered high-frequency sniffing input. *A*: effects on MC and GC firing rates. *B*: effects on MC signal-to-noise ratios. *C*: effects on MC spike latency. *D*: effects on MC spike synchrony. All panels depict averaged results from 10 microcircuit network simulations, each initiated with a different random seed. Error bars denote the standard error of the mean.

ACh and NE modulate GC excitability differently. Although both ACh and NE can alter the intrinsic excitability of GCs, they target different ionic channels and have quite different effects on GC responses to external stimuli. ACh enhances GC excitability by inhibiting two potassium currents, I_M and I_{AHP}, which underlie frequency adaptation and are responsible for generating medium and slow AHP responses (respectively) in GCs. Blockage of these two currents uncovers a Ca^{2+}-activated nonspecific cation current I_{CAN} that transforms the AHP into a sustained ADP (Pressler et al. 2007; Smith and Araneda 2010); the resulting synaptic potentiation requires calcium release from internal stores in the endoplasmic reticulum (Ghatpande et al. 2006). In contrast, NE alters GC excitability nonmonotonically by modulating an ohmic potassium current, I_{KL} (Nai et al. 2010). Low concentrations of NE reduce GC excitability (below that of the unmodulated state) by increasing the I_{KL} conductance, whereas high concentration of NE increases GC excitability by reducing the I_{KL} conductance. One substantial difference between ACh and NE neuromodulation, then, is that ACh can only potentiate GC excitability, whereas NE can either potentiate or reduce GC excitability.

Because the I_{KL} current was much more active than the I_M and I_{AHP} currents in the subthreshold voltage range, NE affects the baseline membrane potential of GCs (and hence the baseline GC firing rate) far more than does ACh (Figs. 4*B* and 5*B*). Also, via graded inhibition, GC membrane potential changes by themselves can effectively alter the degree of inhibition of MCs. In contrast, both I_M and I_{AHP} currents, which are modulated by ACh, require substantial depolarization to activate and strongly regulate the degree of frequency adaptation of GCs. Blocking the I_M and I_{AHP} currents also substantially increased GC input resistance (Pressler et al. 2007). Together, the elimination of frequency adaptation, the increased input resistance, and the conversion of slow AHPs into slow ADPs by ACh strongly enhanced GC firing rates in response to afferent input. In simulations using four different types of afferent input (static current injections, random synaptic inputs, phasic slow respiratory, and tonic filtered sniffing inputs), we consistently found that ACh had a more powerful effect on odor-evoked GC firing rates than did NE.

NE regulates ACh-induced persistent depolarization of GCs. Another major difference between ACh and NE modulation is that ACh can induce sustained depolarization and persistent firing of GCs after transient suprathreshold activity (Figs. 3, 6, and 9), whereas NE generates no comparable persistent effect on high-AHP GCs (see discussion on state-dependent NE effects below). By blocking I_M and I_{AHP} currents, ACh unmasks the I_{CAN} current so that transient depolarization increases Ca^{2+} influx and activates I_{CAN}, leading to a slow ADP current that can support persistent firing. Notably, the ACh-evoked potentiation of GCs requires a sufficiently depolarized baseline membrane potential (Fig. 3*C*) to generate these post-activation effects. Given the relatively hyperpolarized level of GC resting potentials (−68 mV), normal background input in vivo may not be strong enough to depolarize the membrane potential to a baseline level sufficient to enable sustained ADP and persistent firing responses even in the presence of CCh. By effectively modulating the baseline membrane potential, NE could serve to control the expression of persistent depolarization induced by ACh; low concentrations of NE can prevent sustained firing by hyperpolarizing the membrane (Fig. 8*C*), whereas high concentrations of NE can gate or strengthen persistent firing by depolarizing the membrane (Fig. 8*B*).

ACh and NE have different effects on MC firing rates. In the MC-GC microcircuit, we showed that both ACh and NE modulation of GCs could affect MC firing rates but in different ways. By depolarizing GCs, high concentrations of NE inhibited MC spontaneous activity before odor presentation. However, this inhibitory effect of NE was reduced during odor presentation when the I_M and I_{AHP} currents were activated. As a result, high concentrations of NE reduced the baseline MC spike rate but not the odor-evoked MC firing rate, resulting in an improved SNR for afferent MC activation. This SNR improvement is consistent with experimental observations that high concentrations of NE substantially lowered the odorant detection threshold in behaving rats (Escanilla et al. 2010). On the other hand, low concentrations of NE increased the spon-

taneous MC spike rate via GC hyperpolarization while having little effect on the odor-evoked MC firing rates, thus reducing the SNR.

Unlike NE modulation, ACh modulation suppressed the odor-evoked MC firing rate by strongly potentiating GC responses during odor presentation. This suppression effect was greater for the MC receiving relatively weaker odor input. Firing-rate suppression of MCs receiving weaker afferent inputs effectively sharpens the tuning curves of MCs, contributing to the decorrelation of OB odor representations and improving behavioral odor discrimination, as has been demonstrated experimentally and in larger models (Cleland and Sethupathy 2006; D'Souza and Vijayaraghavan 2014; Li and Cleland 2013; Ma and Luo 2012; Mandairon et al. 2006). However, ACh modulation had little effect on the prestimulus spontaneous MC spike rate, resulting in a slight reduction in the single-cell SNR of these sideband-responsive neurons (Figs. 12*C* and 15*C*). The differential effect of ACh and NE modulation on cellular SNR is consistent with experimental findings that noradrenergic, but not cholinergic, modulation of the OB is important for the detection and recognition of low-concentration stimuli (Escanilla et al. 2012). In contrast, ACh modulation substantially reduced MC spontaneous activity after odor stimulation (attributable to ADPs and sustained firing in GCs), whereas NE modulation had little effect on poststimulus spike rates in MCs. Potentially, ACh may serve to progressively sharpen odor representations over time or to reduce the overlap between sequentially presented odors. Combined activation of ACh and higher-concentration NE significantly suppressed MC spontaneous activities both before and after odor presentation and substantially reduced odor-evoked MC firing rates, improving both the SNR and contrast enhancement. On the other hand, one effect of low-concentration NE may be to limit or prevent ACh-induced persistent firing in GCs (Fig. 8*C*), thereby enabling persistent MC firing in response to certain odors (Takahashi et al. 2004).

ACh synchronizes MC spikes more effectively than NE. ACh, via muscarinic receptor activation, has been shown to enhance MC spike synchronization and gamma oscillations in a biophysical OB model (Li and Cleland 2013). Consistent with these results, CCh at all concentrations increased MC spike synchronization in the microcircuit model (Figs. 12*G* and 15*G*). This substantial enhancement of MC spike synchrony was in part a result of the transformation of GC excitatory postsynaptic potentials (EPSPs) into spikes (i.e., a substantial firing-rate increase). Although, with graded synaptic transmission, GC EPSPs could deliver effective inhibition onto MCs, the inhibitory $GABA_A$ conductances induced by GC EPSPs were smaller than the conductances induced by spikes (Fig. 17); this potentiation of phasic inhibition onto MCs by ACh

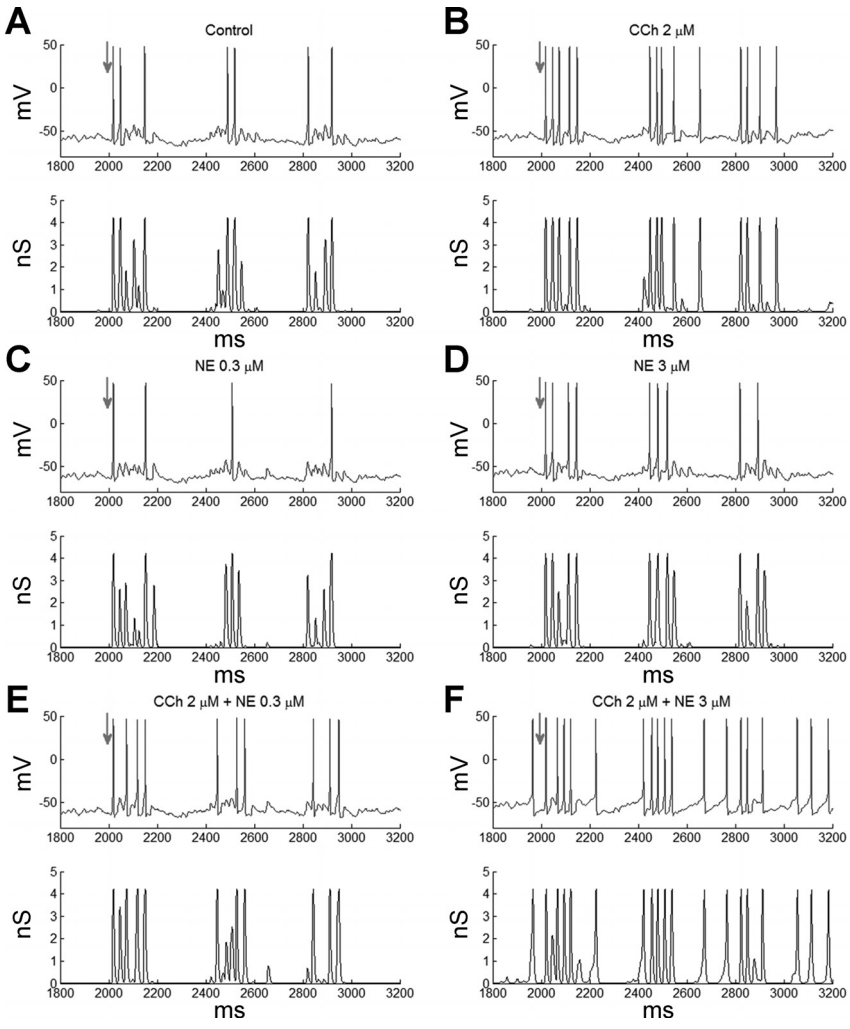

Fig. 17. Voltage responses of a representative GC (*top*) and the conductance of its $GABA_A$-ergic synapse onto an MC (*bottom*) across 3 2.5-Hz (400 ms) respiratory cycles in the MC-GC microcircuit network under the following 6 conditions: control conditions (*A*), CCh (2.0 μM) modulation (*B*), low-NE (0.3 μM) modulation (*C*), high-NE (3.0 μM) modulation (*D*), combined CCh (2.0 μM) and low-NE (0.3 μM) modulation (*E*), combined CCh (2.0 μM) and high-NE (3.0 μM) modulation (*F*). Arrows indicate the onset of the first respiratory cycle.

sharpened MC spike synchronization. In contrast, the synchronization effect induced by NE modulation was considerably weaker; for both respiratory and filtered sniffing inputs, low concentrations of NE slightly reduced MC spike synchrony, whereas high concentrations of NE weakly enhanced MC spike synchrony (Figs. 12*H* and 15*H*). This is because NE had a much smaller effect on GC firing rates than ACh, mainly modulating GC subthreshold voltages. When ACh and NE (in high concentrations) were simultaneously activated, MC spikes were both constrained within a narrow range of the respiratory cycle and strongly synchronized.

Our findings here that the enhancement of inhibition onto MCs by the neuromodulation of GCs improves MC spike synchronization (also see Li and Cleland 2013) contrast with reports from Schoppa and colleagues demonstrating that adrenergic receptor-mediated disinhibition of MCs led to long-term enhancement of synchronized gamma oscillations in the OB (Gire and Schoppa 2008; Pandipati and Schoppa 2012; Pandipati et al. 2010). This discrepancy potentially can be explained by additional established neuromodulator effects, differences in the baseline inhibitory tone, the relative heterogeneity of afferent input levels, and the degree of noise. In our model, ACh and higher concentrations of NE potentiate GC intrinsic excitability and deliver stronger phasic inhibition onto MCs, given a constant synaptic weight (i.e., maximum GABAergic conductance). However, one prominent effect of NE in young rats (<P14) is to reduce GABAergic transmission from GCs to MCs (Pandipati et al. 2010), thereby reducing the inhibitory synaptic weight. In a separate computational study of OB gamma oscillogenesis (G. Li and T. A. Cleland, unpublished observations), we have observed that, although sufficient phasic GC inhibition is required for gamma-band synchronization, excessively large GC→MC synaptic weights impair gamma rhythmicity by oversuppressing MCs, providing a possible explanation for why NE-induced MC disinhibition can result in enhanced gamma oscillatory power. Additionally, the strength of GC inhibition required for optimal MC spike synchronization is tightly linked to the input (or activation) heterogeneity and noise level. If MCs, or a substantial fraction of MCs in a larger network, are relatively homogeneously activated and the noise level is low, the excitatory effect of MC disinhibition will exceed the (small) detrimental effect on synchrony, resulting in an overall increase of oscillatory power. In contrast, in our MC-GC microcircuit model (as in Li and Cleland 2013), the two MCs received substantially different levels of afferent input (Figs. 10 and 14), necessitating stronger GC inhibition for synchronization. Put another way, in the former theoretical case, oscillatory power is activity limited, whereas, in the latter case, it is limited by the strength of phasic inhibition. As with the differences observed between slices taken from rats and mice, relatively modest mechanistic changes in complex systems can generate strongly and qualitatively distinct response properties that disguise their underlying commonalities. It is one of the chief roles of biophysical computational modeling to illustrate these emergent properties and reveal the powerful functional heterogeneity that can be generated by fundamentally similar systems.

NE modulatory effects are state dependent. As discussed earlier, whether ACh induces slow ADPs and persistent firing depends on the depolarization level of GCs and whether and to what extent NE is coactivated. Likewise, the modulatory effects of NE also are state dependent. In our model, GCs expressed high levels of I_M and I_{AHP} conductances in the unmodulated condition, underlying pronounced AHPs and strong frequency adaptation, as observed in rat GCs (Pressler et al. 2007). In such GCs, NE application alone is not able to generate ADP responses or persistent firing (Fig. 3*E*), resulting in relatively weak modulation of GC firing rates (Figs. 2, 5, and 7), again consistent with experimental data from rats (P14-P28; Nai et al. 2010). However, if GCs express much lower levels of I_M and I_{AHP} conductances (as has been observed in slice recordings from P4–P99 mice; Figs. 1 and 3 in Zimnik et al. 2013), NE modulation alone can evoke slow ADPs and quasipersistent firing (Fig. 3*F*), exerting effects similar to those obtained in rat GCs when ACh is simultaneously applied (Fig. 8*B*). These differences may arise from species differences, age, or other experimental variables; notably, expression profiles in the GCs of younger rats (<P14) differ from those in older (>P14) rats such that the net suppressive effects of NE dominate the excitatory effects in the younger animals (Gire and Schoppa 2008; Pandipati and Schoppa 2012; Pandipati et al. 2010), and it is well established that NE modulation in the OB underlies radically different functionality in neonatal rats compared with adults (Landers and Sullivan 2012; Yuan et al. 2014). In each of these cases, the important factor is that the state-dependent expression patterns of local conductances, whether intrinsic or conditional, can dramatically alter the physiological impact of a given neuromodulatory input. This capacity enables powerfully modular regulation of circuit function and highlights the importance of quantitative biophysical modeling approaches to identify the underlying mechanistic commonalities in such functionally dissimilar neural systems.

Limitations of the model. The present model is concerned with the functional differentiation of cholinergic and noradrenergic modulation in OB GCs. MCs in the microcircuit simulations serve as a reasonably realistic assay for the effects of GC neuromodulation on GC functional output, but the direct neuromodulation of MCs was not simulated. Specifically, besides the muscarinic effects on GCs, ACh directly depolarizes MCs via nicotinic receptors (Castillo et al. 1999; D'Souza and Vijayaraghavan 2012; Liu et al. 2015) and also enhances the glomerular layer inhibition of MCs through both nicotinic and muscarinic receptors (Castillo et al. 1999; D'Souza and Vijayaraghavan 2012; D'Souza et al. 2013; Liu et al. 2015). Although not simulated in the present MC-GC microcircuit model, many of these effects have been integrated and examined in a previous OB network model (Li and Cleland 2013). Similar to ACh, NE also directly depolarizes MCs, presumably through modulation of a potassium leak current (Hayar et al. 2001). In addition, both ACh and NE regulate the presynaptic release of GABA from GCs to MCs (Ghatpande et al. 2006; Nai et al. 2009; Pandipati et al. 2010; Zimnik et al. 2013). These effects will certainly further influence the functional modulation of OB processing and could be more thoroughly explored in a fully elaborated OB network model.

Summary. In this biophysical modeling study, we showed that the effects of ACh and NE modulation in OB are both

distinct and complementary to each other. Whereas ACh modulation mainly regulates the firing rates and afterpotentials of GCs, NE modulation mainly regulates GC subthreshold membrane potentials. Combined activation by ACh and NE regulates the induction and expression of persistent firing in GCs after odor stimulus and produces MC output that is more tightly constrained both within the respiratory cycle (theta band) and at the faster timescale of spike synchronization (beta/gamma band). In microcircuit simulations, we further demonstrated that high concentrations of NE improved the neuronal SNR, whereas ACh suppressed odor-evoked MC firing rates and MC spontaneous activity following odor presentation. ACh modulation also synchronized MC spikes more effectively than NE modulation on the beta/gamma time scale, via enhancement of the GC firing frequency and the extended period of inhibition effected by the GC ADP. Simultaneous activation of ACh and (high-concentration) NE concertedly produced strong respiratory phase coupling, a high SNR, and improved spike synchrony among MCs. These findings support the hypothesis that ACh is important for MC spike synchronization and odor discrimination, whereas NE is particularly important for the modulation of the neuronal SNR and potentially also the regulation of cholinergic function.

GRANTS

This work was supported by NIDCD R01 grants DC009948 and DC012249 to T. A. Cleland and NIDCD R03 grant DC013872 to G. Li.

DISCLOSURES

No conflicts of interest, financial or otherwise, are declared by the authors.

AUTHOR CONTRIBUTIONS

Author contributions: G.L. performed experiments; G.L. analyzed data; G.L., C.L., and T.A.C. interpreted results of experiments; G.L. prepared figures; G.L., C.L., and T.A.C. drafted manuscript; G.L., C.L., and T.A.C. edited and revised manuscript; G.L., C.L., and T.A.C. approved final version of manuscript; C.L. and T.A.C. conception and design of research.

REFERENCES

Aston-Jones G, Cohen JD. An integrative theory of locus coeruleus-norepinephrine function: adaptive gain and optimal performance. *Annu Rev Neurosci* 28: 403–450, 2005.

Barkai E, Hasselmo ME. Modulation of the input/output function of rat piriform cortex pyramidal cells. *J Neurophysiol* 72: 644–658, 1994.

Bhalla US, Bower JM. Exploring parameter space in detailed single neuron models: simulations of the mitral and granule cells of the olfactory bulb. *J Neurophysiol* 69: 1948–1965, 1993.

Cadetti L, Belluzzi O. Hyperpolarisation-activated current in glomerular cells of the rat olfactory bulb. *Neuroreport* 12: 3117–3120, 2001.

Cang J, Isaacson JS. In vivo whole-cell recording of odor-evoked synaptic transmission in the rat olfactory bulb. *J Neurosci* 23: 4108–4116, 2003.

Carey RM, Wachowiak M. Effect of sniffing on the temporal structure of mitral/tufted cell output from the olfactory bulb. *J Neurosci* 31: 10615–10626, 2011.

Carnevale NT, Hines ML. *The NEURON Book*. Cambridge, MA: Cambridge University, 2006.

Castillo PE, Carleton A, Vincent JD, Lledo PM. Multiple and opposing roles of cholinergic transmission in the main olfactory bulb. *J Neurosci* 19: 9180–9191, 1999.

Chaudhury D, Escanilla O, Linster C. Bulbar acetylcholine enhances neural and perceptual odor discrimination. *J Neurosci* 29: 52–60, 2009.

Cleland TA, Sethupathy P. Non-topographical contrast enhancement in the olfactory bulb. *BMC Neurosci* 7: 7, 2006.

Cools R, Roberts AC, Robbins TW. Serotoninergic regulation of emotional and behavioural control processes. *Trends Cogn Sci* 12: 31–40, 2008.

de Almeida L, Idiart M, Linster C. A model of cholinergic modulation in olfactory bulb and piriform cortex. *J Neurophysiol* 109: 1360–1377, 2013.

Devore S, Linster C. Noradrenergic and cholinergic modulation of olfactory bulb sensory processing. *Front Behav Neurosci* 6: 52, 2012.

Devore S, Manella LC, Linster C. Blocking muscarinic receptors in the olfactory bulb impairs performance on an olfactory short-term memory task. *Front Behav Neurosci* 6: 59, 2012.

Doucette W, Milder J, Restrepo D. Adrenergic modulation of olfactory bulb circuitry affects odor discrimination. *Learn Mem* 14: 539–547, 2007.

D'Souza RD, Vijayaraghavan S. Nicotinic receptor-mediated filtering of mitral cell responses to olfactory nerve inputs involves the $\alpha 3\beta 4$ subtype. *J Neurosci* 32: 3261–3266, 2012.

D'Souza RD, Vijayaraghavan S. Paying attention to smell: cholinergic signaling in the olfactory bulb. *Front Synaptic Neurosci* 6: 21, 2014.

D'Souza RD, Parsa PV, Vijayaraghavan S. Nicotinic receptors modulate olfactory bulb external tufted cells via an excitation-dependent inhibitory mechanism. *J Neurophysiol* 110: 1544–1553, 2013.

Escanilla O, Arrellanos A, Karnow A, Ennis M, Linster C. Noradrenergic modulation of behavioral odor detection and discrimination thresholds in the olfactory bulb. *Eur J Neurosci* 32: 458–468, 2010.

Escanilla O, Alperin S, Youssef M, Ennis M, Linster C. Noradrenergic but not cholinergic modulation of olfactory bulb during processing of near threshold concentration stimuli. *Behav Neurosci* 126: 720–728, 2012.

Fletcher ML, Chen WR. Neural correlates of olfactory learning: Critical role of centrifugal neuromodulation. *Learn Mem* 17: 561–570, 2010.

Ghatpande AS, Sivaraaman K, Vijayaraghavan S. Store calcium mediates cholinergic effects on mIPSCs in the rat main olfactory bulb. *J Neurophysiol* 95: 1345–1355, 2006.

Gire DH, Schoppa NE. Long-term enhancement of synchronized oscillations by adrenergic receptor activation in the olfactory bulb. *J Neurophysiol* 99: 2021–2025, 2008.

Hayar A, Heyward PM, Heinbockel T, Shipley MT, Ennis M. Direct excitation of mitral cells via activation of α1-noradrenergic receptors in rat olfactory bulb slices. *J Neurophysiol* 86: 2173–2182, 2001.

Hines ML, Carnevale NT. The NEURON simulation environment. *Neural Comput* 9: 1179–1209, 1997.

Hodgkin AL, Huxley AF. A quantitative description of membrane current and its application to conduction and excitation in nerve. *J Physiol* 117: 500–544, 1952.

Inoue T, Strowbridge BW. Transient activity induces a long-lasting increase in the excitability of olfactory bulb interneurons. *J Neurophysiol* 99: 187–199, 2008.

Landers MS, Sullivan RM. The development and neurobiology of infant attachment and fear. *Dev Neurosci* 34: 101–114, 2012.

Li G, Cleland TA. A two-layer biophysical model of cholinergic neuromodulation in olfactory bulb. *J Neurosci* 33: 3037–3058, 2013.

Linster C, Cleland TA. Cholinergic modulation of sensory representations in the olfactory bulb. *Neural Netw* 15: 709–717, 2002.

Linster C, Nai Q, Ennis M. Nonlinear effects of noradrenergic modulation of olfactory bulb function in adult rodents. *J Neurophysiol* 105: 1432–1443, 2011.

Liu S, Shao Z, Puche A, Wachowiak M, Rothermel M, Shipley MT. Muscarinic receptors modulate dendrodendritic inhibitory synapses to sculpt glomerular output. *J Neurosci* 35: 5680–5692, 2015.

Madison DV, Lancaster B, Nicoll RA. Voltage clamp analysis of cholinergic action in the hippocampus. *J Neurosci* 7: 733–741, 1987.

Ma M, Luo M. Optogenetic activation of basal forebrain cholinergic neurons modulates neuronal excitability and sensory responses in the main olfactory bulb. *J Neurosci* 32: 10105–10116, 2012.

Mandairon N, Linster C. Odor perception and olfactory bulb plasticity in adult mammals. *J Neurophysiol* 101: 2204–2209, 2009.

Mandairon N, Ferretti CJ, Stack CM, Rubin DB, Cleland TA, Linster C. Cholinergic modulation in the olfactory bulb influences spontaneous olfactory discrimination in adult rats. *Eur J Neurosci* 24: 3234–3244, 2006.

Mandairon N, Peace S, Karnow A, Kim J, Ennis M, Linster C. Noradrenergic modulation in the olfactory bulb influences spontaneous and reward-motivated discrimination, but not the formation of habituation memory. *Eur J Neurosci* 27: 1210–1219, 2008.

McLean JH, Shipley MT, Nickell WT, Aston-Jones G, Reyher CK. Chemoanatomical organization of the noradrenergic input from locus coer-

uleus to the olfactory bulb of the adult rat. *J Comp Neurol* 285: 339–349, 1989.

Migliore M, Shepherd GM. Dendritic action potentials connect distributed dendrodendritic microcircuits. *J Comput Neurosci* 24: 207–221, 2008.

Migliore M, Hines ML, Shepherd GM. The role of distal dendritic gap junctions in synchronization of mitral cell axonal output. *J Comput Neurosci* 18: 151–161, 2005.

Nai Q, Dong HW, Hayar A, Linster C, Ennis M. Noradrenergic regulation of GABAergic inhibition of main olfactory bulb mitral cells varies as a function of concentration and receptor subtype. *J Neurophysiol* 101: 2472–2484, 2009.

Nai Q, Dong HW, Linster C, Ennis M. Activation of alpha1 and alpha2 noradrenergic receptors exert opposing effects on excitability of main olfactory bulb granule cells. *Neuroscience* 169: 882–892, 2010.

Pandipati S, Schoppa NE. Age-dependent adrenergic actions in the main olfactory bulb that could underlie an olfactory sensitive period. *J Neurophysiol* 108: 1999–2007, 2012.

Pandipati S, Gire DH, Schoppa NE. Adrenergic receptor-mediated disinhibition of mitral cells triggers long-term enhancement of synchronized oscillations in the olfactory bulb. *J Neurophysiol* 104: 665–674, 2010.

Pinato G, Midtgaard J. Regulation of granule cell excitability by a low-threshold calcium spike in turtle olfactory bulb. *J Neurophysiol* 90: 3341–3351, 2003.

Pressler RT, Inoue T, Strowbridge BW. Muscarinic receptor activation modulates granule cell excitability and potentiates inhibition onto mitral cells in the rat olfactory bulb. *J Neurosci* 27: 10969–10981, 2007.

Ravel N, Akaoka H, Gervais R, Chouvet G. The effect of acetylcholine on rat olfactory bulb unit activity. *Brain Res Bull* 24: 151–155, 1990.

Sarter M, Bruno JP. Cognitive functions of cortical acetylcholine: toward a unifying hypothesis. *Brain Res Brain Res Rev* 23: 28–46, 1997.

Sarter M, Hasselmo ME, Bruno JP, Givens B. Unraveling the attentional functions of cortical cholinergic inputs: interactions between signal-driven and cognitive modulation of signal detection. *Brain Res Brain Res Rev* 48: 98–111, 2005.

Schoppa NE. Synchronization of olfactory bulb mitral cells by precisely timed inhibitory inputs. *Neuron* 49: 271–283, 2006.

Schoppa NE, Westbrook GL. Regulation of synaptic timing in the olfactory bulb by an A-type potassium current. *Nat Neurosci* 2: 1106–1113, 1999.

Schultz W, Dayan P, Montague PR. A neural substrate of prediction and reward. *Science* 275: 1593–1599, 1997.

Smith RS, Araneda RC. Cholinergic modulation of neuronal excitability in the accessory olfactory bulb. *J Neurophysiol* 104: 2963–2974, 2010.

Takahashi YK, Nagayama S, Mori K. Detection and masking of spoiled food smells by odor maps in the olfactory bulb. *J Neurosci* 24: 8690–8694, 2004.

Usher M, Cohen JD, Servan-Schreiber D, Rajkowski J, Aston-Jones G. The role of locus coeruleus in the regulation of cognitive performance. *Science* 283: 549–554, 1999.

Verhagen JV, Wesson DW, Netoff TI, White JA, Wachowiak M. Sniffing controls an adaptive filter of sensory input to the olfactory bulb. *Nat Neurosci* 10: 631–639, 2007.

Wang XJ. Fast burst firing and short-term synaptic plasticity: a model of neocortical chattering neurons. *Neuroscience* 89: 347–362, 1999.

Wang XJ, Buzsáki G. Gamma oscillation by synaptic inhibition in a hippocampal interneuronal network model. *J Neurosci* 16: 6402–13, 1996.

Yuan Q, Shakhawat AM, Harley CW. Mechanisms underlying early odor preference learning in rats. *Prog Brain Res* 208: 115–156, 2014.

Záborszky L, Carlsen J, Brashear HR, Heimer L. Cholinergic and GABAergic afferents to the olfactory bulb in the rat with special emphasis on the projection neurons in the nucleus of the horizontal limb of the diagonal band. *J Comp Neurol* 243: 488–509, 1986.

Zador A, Koch C, Brown TH. Biophysical model of a Hebbian synapse. *Proc Natl Acad Sci USA* 87: 6718–22, 1990.

Zimnik NC, Treadway T, Smith RS, Araneda RC. α(1A)-Adrenergic regulation of inhibition in the olfactory bulb. *J Physiol* 591: 1631–1643, 2013.